

3D COMPOSITE FINITE ELEMENTS FOR ELLIPTIC BOUNDARY VALUE PROBLEMS WITH DISCONTINUOUS COEFFICIENTS

TOBIAS PREUSSER*, MARTIN RUMPF†, STEFAN SAUTER‡, AND
LARS OLE SCHWEN†

Abstract. For scalar and vector-valued elliptic boundary value problems with discontinuous coefficients across geometrically complicated interfaces, a composite finite element approach is developed. Composite basis functions are constructed, mimicking the expected jump condition for the solution at the interface in an approximate sense. The construction is based on a suitable local interpolation on the space of admissible functions. We study the order of approximation and the convergence properties of the method numerically. As applications, heat diffusion in an aluminium foam matrix filled with polymer and linear elasticity of micro-structured materials, in particular specimens of trabecular bone, are investigated. Furthermore, a numerical homogenization approach is developed for periodic structures and real material specimens which are not strictly periodic but are considered as statistical prototypes. Thereby, effective macroscopic material properties can be computed.

Key words. composite finite elements, homogenization, elliptic partial differential equations, discontinuous coefficients

AMS subject classifications. 65M60, 65N30, 74S05, 74Q05, 80M40

1. Introduction. Simulations in materials science or bio-medical applications are frequently faced with multi-phase materials having interfaces of complicated structure. Examples are heat conduction in chip design [28], the elastic behavior of composite materials [62], electric fields in the human body [88] in the context of electrocardiography [32], the brain shift in neurosurgery [85], and effects of vertebroplasty on macroscopic properties of trabecular microstructure [47]. The standard finite element (FE) procedure in this context is to generate a geometrically complicated simplicial (i.e. triangular or tetrahedral in 2D or 3D, respectively) FE mesh that resolves the interface between the different materials. On these meshes standard FE basis functions are used for the discretization of the physical quantities. However, generating 3D meshes suitable for FE simulations is difficult [13, 77, 71] and may require substantial user interaction.

Review of Related Methods. Besides the classical meshing, a variety of alternative approaches has been investigated. Interfaces to be dealt with in simulations can occur as interfaces between ‘domain’ and ‘void’ or between two different ‘(sub-)domains’ with different material properties. The idea of modifying finite difference stencils near boundaries goes back to [72]. A similar method for the case of discontinuous coefficients is the *Immersed Interface Method* (IIM) that is based on the idea of using finite differences on Cartesian grids and adapting the stencils near the interface. The IIM for 1D/2D problems with discontinuous coefficients and possibly singular sources on the interface is discussed in [14, 48]. It is extended to 3D in [49] and combined with level set methods in [70]. A multigrid solver for the IIM is introduced in [1], [51] is an overview of IIM applications. The IIM is combined with a finite volume method using ‘capacity functions’ for partially filled cells in [16], it is modified to the *Explicit*

*Fraunhofer MEVIS, Bremen, Germany; School of Engineering and Science, Jacobs University Bremen, Germany, tobias.preusser@mevis.fraunhofer.de

†Institute for Numerical Simulation, University of Bonn, Germany,
{[martin.rumpf](mailto:martin.rumpf@ins.uni-bonn.de),[ole.schwen](mailto:ole.schwen@ins.uni-bonn.de)}@ins.uni-bonn.de

‡Institut für Mathematik, Universität Zürich, Switzerland, stas@math.uzh.ch

Jump IIM [84] considering not only the discontinuities in the coefficient but also the expected singularities in the solution.

The bridge to the FE world for 1D and 2D problems is built by ‘Immersed Finite Elements’ [50, 52]. The *Partition of Unity Method* (PUM) combines a finite partition of unity covering of the object with a priori knowledge about the behavior of the solution at the interface [8]. The *Generalized Finite Element Method* [56, 21, 7] is per se a meshless method and was also developed under the name *hp clouds* [59]. It was combined with classical FE to improve their approximation capabilities [22, 74, 23]. The *Extended Finite Element Method* (XFEM) [12] uses classical FE and ‘enriches’ them by additional basis functions to incorporate discontinuities. The enrichment introduces additional degrees of freedom even though the meshes are independent of the location of discontinuities. A major application is the simulation of crack propagation [19, 73, 45] where frequent remeshing in classical methods [11] can be avoided by using XFEM. The *Fictitious Domain Method* [46, 66, 6, 30, 63] uses a domain-independent mesh for a superset of the computational domain on which the partial differential equation being considered is extended appropriately. This approach has been combined with the p version of FE for 2D and 3D problems in [61] and [24], respectively. *Weighted Extended B-Splines* (WEB splines) [41, 40] use tensor products of splines on regular grids multiplied by weight functions for an adaptation to the geometric boundary. WEB splines are particularly well suited for domains constructed via computer-aided design approaches. *Unfitted meshes* have been analyzed for problems on curved domains [10] and for discontinuous coefficients across curved interfaces [9, 38]. Here, FE basis functions are restricted via appropriate quadrature rules to the actual computational domains which may be described by a level set function.

Composite Finite Elements. Composite finite elements (CFE) are based on the idea of incorporating the geometric complexity of physical domains [36, 35, 37, 64] or interfaces between subdomains with different material properties [67] into the shape of basis functions rather than in the FE mesh. A corresponding multigrid method has been investigated in [67]. The term ‘composite’ has also appeared in the FE literature in *Composite Triangles* [33, 78]. Like our approach presented here, these methods also use a virtual subdivision of tetrahedral elements, however, not as an adaptation to the geometry of the underlying domains.

The approach presented in this paper is based on work of Sauter and Hackbusch [67] for 2D problems. A corresponding CFE approach for complicated single-phase domains is investigated in [53] and applied in a homogenization framework in [69]. In this paper, we focus on the construction of the CFE basis in case of 3D, isotropic and anisotropic heat diffusion and of 3D linear elasticity. For the 2D cases and a corresponding derivation in full detail, we refer to [68].

Our approach takes into account interfaces which are described on a fine mesh via a level set function. Hence, the resulting computational tool is tailored to the simulation on multi-phase domains, where the domains are described via 3D images resulting e.g. from MRI or CT scans of objects. While the general CFE method can effectively be combined with an adaptive mesh refinement (see e.g. [57, 25]), in our case the domain description via image data naturally defines the finest computational mesh as the one associated with the 3D image data. Far from the interface, the CFE basis functions of our approach coincide with the standard basis functions on an overlaid structured grid. In the vicinity of the interface, the standard basis is modified to meet suitable coupling conditions at the interface. This is achieved by

an interpolation operator that evaluates admissible functions on the interface. A function is admissible if it satisfies the problem-specific coupling condition across the interface which follows from the flux or stress balance. Temporarily, a local auxiliary mesh is considered in the assembly of local stiffness and mass matrices, where the interpolation is encoded via weights for piecewise affine functions on this local fine mesh. Our efficient algorithm for the local resolution of the interface via a conforming tetrahedral mesh is inspired by the marching cubes [54] and marching tetrahedra [79] algorithms. Lookup tables classify all possible topological variants, thus making the local conforming tetrahedral mesh for the resolution of the interface completely virtual. In the global matrix-assembly, appropriately scaled pre-computed values are retrieved from the lookup tables.

Homogenization. For a microscopically inhomogeneous but macroscopically homogeneous material, ‘homogenization’ [76] or ‘upscaling’ [4, 83] methods allow to determine effective material properties to be used e.g. in single-scale purely macroscopic or in two-scale FE simulations [44, 3, 55]. Multigrid coarsening strategies for upscaling have been proposed in [58, 5, 15].

Determining effective elastic properties of microstructured (but not necessarily periodic) cellular solids has for instance been studied in biomechanics in [42, 29] where the unit cells are referred to as ‘representative volume elements’ [43] or ‘representative elementary volumes’ [31]. In biomechanics, FE simulations are used for the development and assessment of treatment techniques for vertebral fractures [18, 65] and implants for osteoporotic bones [17], where a proper knowledge of macroscopic parameters is needed for continuum models. In these applications, full-scale resolution of the bone microstructure requires huge amounts of computational resources [81]. For microstructured elastic objects, one studies a ‘cell problem’ [2, Chapter 1], which is supposed to generate a periodic lattice. Then, based on a suitable set of computations with uniaxial loading, one can evaluate the homogenized (macroscopic) elasticity tensor. For first results restricted to the case of periodic complicated domains we refer to [69].

A particular focus in this paper is on microstructures which are not exactly periodic but statistically characteristic specimens of a material, which is the usual case for most real world specimens. Here, we propose a variant of the classical cell problem in homogenization replacing periodic boundary conditions by appropriate Dirichlet boundary conditions. The evaluation of stresses is restricted to a cell which is a subset of the computational domain with sufficient distance from the boundary of the specimen. We experimentally study the reliability of this approach and for example show that the usual size of trabecular bone specimens indeed allows the identification of macroscopic elastic properties of the bone microstructure.

Paper Outline. Section 2 discusses the class of problems suitable for our approach. The construction of the CFE basis is presented in Section 3 for the isotropic scalar case and then extended to the anisotropic scalar case and the vector-valued case. Details about the implementation are discussed in Section 4 and numerical results are presented in Section 5. The homogenization is discussed in detail in Section 6, where results are presented as well.

2. Interface Description and Coupling Conditions. In this section we introduce level set descriptions of material interfaces in the computational domain and investigate associated coupling conditions, both for scalar and vector-valued problems.

We will explain our concepts for the unit cube $\Omega := (0, 1)^3$, which is decomposed

in two subdomains Ω_{\pm} and an interface γ , where

$$\Omega_+ := \{x \in \Omega \mid \varphi(x) > 0\}, \quad \Omega_- := \{x \in \Omega \mid \varphi(x) < 0\}, \quad \gamma := \{x \in \Omega \mid \varphi(x) = 0\},$$

and where $\varphi : \Omega \rightarrow \mathbb{R}$ is a (non-degenerate) level set function [60]. Thus we have $\bar{\Omega} = \bar{\Omega}_+ \cup \bar{\Omega}_-$ and the (*material*) *interface* is given as $\gamma = \Omega \cap (\bar{\Omega}_+ \cap \bar{\Omega}_-)$.

Typically, φ is given as voxel image data interpreted as nodal values on a uniform grid or as elements of a piecewise multi-linear FE space on a regular hexahedral mesh. Thus, φ is supposed to be continuously differentiable a.e. and non-degenerate in the sense that $\nabla\varphi(z) \neq 0$ on γ . Let $n := |\nabla\varphi(z)|^{-1}\nabla\varphi(z)$ denote the normal direction to the interface and s, t two tangential directions such that n, s, t are pairwise orthogonal and normalized. Hence the gradient of a differentiable scalar-valued function $u : \Omega \rightarrow \mathbb{R}$ can be represented as

$$\nabla u = \partial_n u n + \partial_s u s + \partial_t u t, \quad (2.1)$$

where $\partial_n u = \nabla u \cdot n$, $\partial_s u = \nabla u \cdot s$, and $\partial_t u = \nabla u \cdot t$. We will extensively use this local coordinate system for the construction of CFE basis functions.

Let us finally note that the extension to more general $\Omega \subset \mathbb{R}^3$ or multiple subdomains is possible. Also note that a single level set function as used here allows for multiple subdomains, but rules out triple lines (T-junctions).

2.1. Scalar Elliptic Problem. We consider the scalar elliptic boundary value problem in weak form

$$\int_{\Omega} a \nabla u \cdot \nabla v \, dx = \int_{\Omega} f v \, dx \quad \forall v \in H_0^{1,2}(\Omega) \quad (2.2)$$

for a right hand side $f \in L^2(\Omega)$ and a second order tensor a in the general anisotropic case or (for notational simplicity) a scalar function in the isotropic case. As usual, $H_0^{1,2}(\Omega)$ denotes the Sobolev space of functions with weak derivatives bounded in L^2 and vanishing trace on $\partial\Omega$. We assume $a(x)$ to be symmetric for each $x \in \Omega$, and bounded such that $\alpha_1 \geq a(x) \xi \cdot \xi \geq \alpha_0 > 0$ for all $\xi \in \mathbb{R}^3$, $|\xi| = 1$. For the ease of the presentation we assume a to be constant on the subdomains, $a|_{\Omega_{\pm}} =: a^{\pm}$.

Conservation of energy at a point z on the interface implies continuity of the normal flux $a \nabla u \cdot n$ across the interface and continuity of u and thus, under suitable smoothness assumptions, its derivatives in the tangential directions s and t . Weak solutions satisfy the physically relevant interfacial coupling condition $[a \nabla u \cdot n]_{\gamma} = 0$ a.e. on γ . Here and in the following, $[\cdot]_{\gamma}$ denotes the jump across the interface, i.e. $[a \nabla u \cdot n]_{\gamma}(z) := (a \nabla u \cdot n)^+(z) - (a \nabla u \cdot n)^-(z)$, where

$$g^{\pm}(z) := \lim_{\Omega_{\pm} \ni x \rightarrow z} g(x) \quad (2.3)$$

for any scalar or vector-valued function g on Ω .

Moreover the solution to (2.2) piecewise solves sub-problems with continuous coefficients on the sub-domains Ω_{\pm} . Consequently for the construction of the CFE space we introduce the vector space of admissible functions being continuous across the interface, respecting the coupling condition, and fulfilling $-\operatorname{div}(a^{\pm} \nabla u) \in L^2(\Omega_{\pm})$ on both sides of the interface

$$\mathcal{V} := \left\{ u \in H_0^{1,2}(\Omega) \mid \operatorname{div}(a^{\pm} \nabla u|_{\Omega_{\pm}}) \in L^2(\Omega_{\pm}), [u]_{\gamma} = 0 = [a \nabla u \cdot n]_{\gamma} \right\}. \quad (2.4)$$

For this space we will deduce a local discrete counterpart in the construction of our composite finite element function space.

In the *isotropic case* where a can be viewed as a scalar, we can define the *kink ratio* $\kappa := a^-/a^+$. For a 1D diffusion problem κ is the ratio between the slopes of the solution on both sides.

For the general *anisotropic case* we rewrite the interface conditions as continuity of u at z and

$$a^- \nabla u^-(z) \cdot n = a^+ \nabla u^+(z) \cdot n. \quad (2.5)$$

Taking into account the decomposition of the normal flux via (2.1),

$$a \nabla u \cdot n = \partial_n u (a n \cdot n) + \partial_s u (a s \cdot n) + \partial_t u (a t \cdot n), \quad (2.6)$$

we immediately verify that the Gâteaux derivatives of u on both sides of the interface are coupled by the following linear system of equations (also taking into account the continuity of the tangential components of ∇u)

$$\begin{pmatrix} \partial_n u^+ \\ \partial_s u^+ \\ \partial_t u^+ \end{pmatrix} = \begin{pmatrix} K^n & K^s & K^t \\ 0 & 1 & 0 \\ 0 & 0 & 1 \end{pmatrix} \begin{pmatrix} \partial_n u^- \\ \partial_s u^- \\ \partial_t u^- \end{pmatrix} \quad (2.7)$$

with

$$K^n = \frac{a^- n \cdot n}{a^+ n \cdot n}, \quad K^s = \frac{(a^- - a^+) s \cdot n}{a^+ n \cdot n}, \quad K^t = \frac{(a^- - a^+) t \cdot n}{a^+ n \cdot n}.$$

The denominator is nonzero because a^+ is strictly positive definite. Hence in the anisotropic diffusion case, the coupling of the derivatives across the interface is not merely represented by a simple kink but reflects an interplay of normal and tangential components of the diffusion tensor a .

2.2. Linearized Elasticity in 3D. To consider linearized elasticity, we introduce the (symmetrized) strain tensor $\epsilon(u) = \frac{1}{2} [Du + (Du)^T]$ for a displacement $u : \mathbb{R}^3 \rightarrow \mathbb{R}^3$ and the elliptic operator

$$u \mapsto -\operatorname{div}(C\epsilon(u)), \quad (2.8)$$

which is supposed to be interpreted in the weak sense on $H^{1,2}(\mathbb{R}^3, \mathbb{R}^3)$. Here, $C = (C_{ijkl})_{ijkl=0,\dots,3}$ denotes the spatially varying fourth-order linear elasticity tensor which satisfies the usual symmetry assumptions $(C_{ijkl} = C_{jikl} = C_{ijlk} = C_{klji})$ and the ellipticity estimate $\sum_{ijkl} C_{ijkl} \xi_{ij} \xi_{kl} \geq \alpha \|\xi\|_F^2$ with $\alpha > 0$ for all $\xi \in \mathbb{R}^{3 \times 3}$, where $\|\cdot\|_F$ denotes the Frobenius norm.

Elasticity tensors are defined in terms of Young's modulus $E > 0$ and Poisson's ratio $\nu \in (-1, 0.5)$, which lead to the Lamé numbers $\lambda = \frac{E\nu}{(1+\nu)(1-2\nu)}$, $\mu = \frac{E}{2(1+\nu)}$ such that $C_{ijkl} = \lambda(\delta_{ij}\delta_{kl}) + \mu(\delta_{il}\delta_{jk} + \delta_{ik}\delta_{jl})$.

The equilibrium configuration of an elastic solid is characterized by the continuity of the normal stress $C\epsilon(u)n$ and the continuity of the displacement u . This leads to the linear system of equations for a point z on the interface (cf. (2.5))

$$C^+ \epsilon(u^+(z))n = C^- \epsilon(u^-(z))n, \quad (2.9)$$

where $C\epsilon(u)n = (\sum_{ijkl} C_{ijkl} \epsilon(u(x))_{kl} n_j)_{i=0,1,2}$. In analogy to the scalar case above we can express the relation between Du^- and Du^+ by the 9×9 block structured

linear system (also taking into account the continuity of the directional derivatives in tangential direction $\partial_s u = Du s$, $\partial_t u = Du t$, cf. (2.7))

$$\begin{pmatrix} \partial_n u^+ \\ \partial_s u^+ \\ \partial_t u^+ \end{pmatrix} = \begin{pmatrix} K^n & K^s & K^t \\ 0 & 1 & 0 \\ 0 & 0 & 1 \end{pmatrix} \begin{pmatrix} \partial_n u^- \\ \partial_s u^- \\ \partial_t u^- \end{pmatrix}. \quad (2.10)$$

Here $\partial_n u^\pm = Du^\pm n$, $\partial_s u^\pm = Du^\pm s$, $\partial_t u^\pm = Du^\pm t \in \mathbb{R}^3$, $K^n, K^s, K^t \in \mathbb{R}^{3 \times 3}$ with K^n being invertible. An explicit form of these matrices is given in [68]. Furthermore, $0, 1$ are the zero and identity matrix in $\mathbb{R}^{3 \times 3}$, respectively.

We need to verify that the relation (2.10) actually holds, or in other words that for given Du^- , the condition (2.9) can be rewritten in the form (2.10). Hence, it is sufficient to demonstrate that, given the coupling conditions, $Du^- = 0$ implies that $Du^+ = 0$. At first, we observe that $\partial_s u^+ = \partial_t u^+ = 0$ because of $\partial_s u^- = \partial_t u^- = 0$. Hence, $Du^+(x) = wn^T$ for some $w = w(x) \in \mathbb{R}^3$. Furthermore, from the continuity of the normal stress we deduce that $C^-\epsilon(u^-)n = 0$. Scalar multiplication of this equation by w leads to

$$\begin{aligned} 0 &= (C^-\epsilon(u^-)n) \cdot w = \sum_i \left(\sum_{jkl} C_{ijkl}^+ \epsilon(u^+)_{kl} n_j \right) w_i \\ &= \sum_i \left(\sum_{jkl} C_{ijkl}^+ (Du^+)_{kl} n_j \right) w_i = \sum_{ijkl} C_{ijkl}^+ w_k n_l w_i n_j \geq \alpha \|wn^T\|_F^2, \end{aligned}$$

where we have used the symmetry assumption and the ellipticity estimate for the tensor C . Hence $wn^T = 0$, from which $w = 0$ and thus $Du^+ = 0$ immediately follow.

3. Construction of Interface-Sensitive Basis Functions. The notation and terminology used in this section follow [53], where a similar basic methodology is used and introduced for the construction of CFE on complicated domains with continuous coefficients. Starting from standard affine FE basis functions on a uniform mesh, our aim is to construct CFE basis functions associated with the same nodes such that the corresponding nodal interpolation of a function satisfies the appropriate coupling conditions (2.5) or (2.9) across the interface. For this purpose, we first define a local auxiliary tetrahedral mesh that resolves a piecewise planar approximation of the interface and define CFE basis functions as a weighted sum of standard affine basis functions on this local auxiliary mesh. Our construction is characterized by the following properties:

(i) The CFE basis consists of nodal basis functions, whose nodes coincide with the vertices of the uniform hexahedral grid.

(ii) Far from the interface, the CFE basis functions are classical piecewise affine nodal basis functions. In the vicinity of the interface, they are composed of affine functions on the local auxiliary submesh which only contains ‘slave’ nodes [26], with fixed interpolation weights depending solely on the geometry of the local auxiliary mesh and on a^\pm or C^\pm , respectively.

(iii) The CFE basis functions have local support, which can be slightly larger than the standard support of the piecewise affine basis functions.

3.1. Regular Grids and Local Auxiliary Meshes. In this section, we start from a regular tetrahedral mesh and construct the local auxiliary mesh. Based on this, we define the CFE basis functions in the scalar and the vector-valued case.

At first, we take into account a *regular hexahedral* grid \mathcal{G}^\square discretizing $\bar{\Omega} = [0, 1]^3$ by 2^{3l} elements, where $h_l = 2^{-l}$ is the resulting grid width and $(2^l + 1)^3$ the number

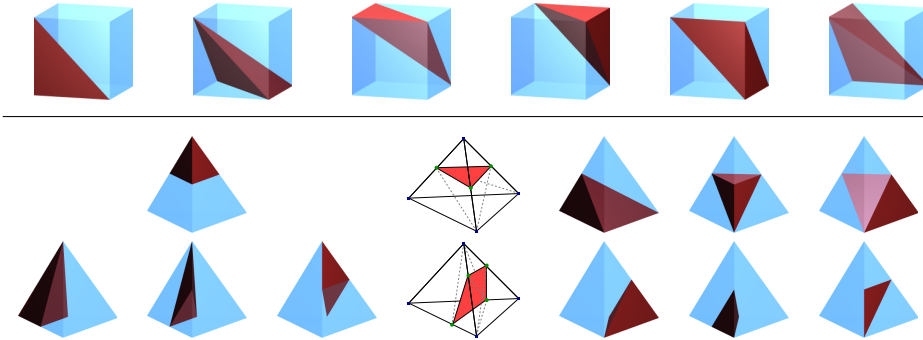


FIG. 3.1. The six tetrahedra of a subdivided hexahedron are shown in the top row. Angles between edges of these regular tetrahedra are bounded from above by 90° . Furthermore, the splitting of a tetrahedron into one pentahedron and one tetrahedron (middle row) or two pentahedra (bottom) and the further subdivision into tetrahedra is depicted. Each pentahedron has two triangular faces and three quadrilateral faces for which the subdivision of two neighboring pentahedra needs to be consistent.

of nodes. The set of vertices of the mesh \mathcal{G}^\square is denoted by \mathcal{N}^\square . It turns out to be more convenient to deal with piecewise affine functions instead of piecewise trilinear ones, which would be the canonical choice for hexahedral grids. Hence, we assume each hexahedron to be subdivided into 6 tetrahedra (cf. Fig. 3.1 and [53]) in such a way that the subdivision is consistent with neighboring cubes. Let us denote this *regular tetrahedral* mesh by \mathcal{G}^\boxtimes and the set of vertices by \mathcal{N}^\boxtimes , which by construction coincides with the vertex set of \mathcal{G}^\square , i.e. $\mathcal{N}^\boxtimes = \mathcal{N}^\square$. On this mesh we define the classical piecewise affine FE space \mathcal{V}^\boxtimes with the nodal projection Π^\boxtimes and the nodal basis functions ψ_i^\boxtimes with $\psi_i^\boxtimes(x_j) = \delta_{ij}$ for the nodes $x_j \in \mathcal{N}^\boxtimes$. Furthermore, let us denote the corresponding nodal index set by $I^\square \subset \mathbb{N}$.

Construction of the Local Auxiliary Mesh. Let $\varphi^\boxtimes := \Pi^\boxtimes \varphi$ be the piecewise affine approximation of the levelset function φ describing the interface. This yields a piecewise planar approximation of the interface $\gamma^\boxtimes := \{x \in \Omega \mid \varphi^\boxtimes(x) = 0\}$ and corresponding domains Ω_\pm^\boxtimes . To avoid degeneracies in the following construction we assume that intersections of γ^\boxtimes with \mathcal{G}^\boxtimes lie at least a small fraction of the grid spacing ('safety margin') away from the grid nodes. This necessary modification of φ is of the same order of magnitude as the measurement and segmentation errors introduced by the image acquisition for φ using CT or MRI. Each tetrahedron in \mathcal{G}^\boxtimes intersected by γ^\boxtimes is split in two polyhedra which are again split in subtetrahedra, (cf. Fig. 3.1), where the splitting of two neighboring polyhedra needs to be consistent. Thereby, we obtain the *local auxiliary mesh* \mathcal{G}^Δ consisting solely of tetrahedral elements.

Virtual Nodes and Virtual Basis Functions. We denote the standard piecewise affine basis function of the space \mathcal{V}^Δ of piecewise affine functions on \mathcal{G}^Δ by $(\psi_i^\Delta)_i$ and call them *virtual basis functions*. The set of nodes of \mathcal{G}^Δ is denoted by \mathcal{N}^Δ and we call $\gamma^\boxtimes \cap \mathcal{N}^\Delta = \mathcal{N}^\Delta \setminus \mathcal{N}^\square$ the set of *virtual nodes* (cf. Fig. 3.2).

Let us remark that γ^\boxtimes is a subset of tetrahedral faces of \mathcal{G}^Δ . Furthermore, note that the topology of the splitting is uniquely determined by the sign of the level set function φ at the vertices, whereas the geometry of the subdivision depends on the actual values of φ at nearby vertices.

3.2. Composite Basis Functions for a Scalar Problem. The construction of the CFE basis requires a suitable interpolation operator $\mathcal{I} : C^0 \rightarrow \mathcal{V}^\Delta$, which

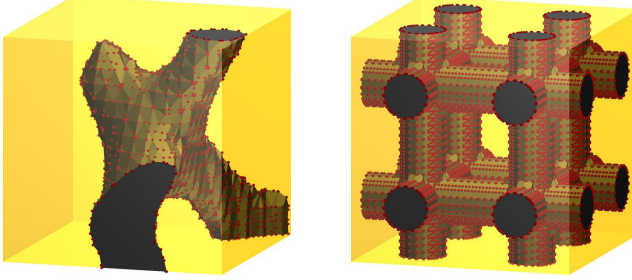


FIG. 3.2. Virtual nodes on part of a trabecular aluminium structure at resolution 17^3 and an artificial rod dataset at resolution 33^3 are depicted as little red spheres. For the construction of the local auxiliary mesh, γ has been approximated by γ^{\boxtimes} and thus appears non-smoothly shaded in the image. The underlying hexahedral grid and the location of virtual nodes on its edges and some of its diagonals is clearly visible from the left picture.

delivers nodal values at the virtual interface nodes. These need to be consistent with the interfacial coupling condition (2.5) or (2.9). Indeed, for a planar interface, $\mathcal{I}[u] = u$ shall hold for any function u which is piecewise affine on both sides of the interface and fulfills the coupling condition at the interface.

Local Interpolation Scheme. At first, we construct such an interpolation locally on a tetrahedron $T \in \mathcal{G}^{\boxtimes}$ for a virtual node z and an interface-normal $n = n(z) \in \mathbb{R}^3$ (the corresponding tangential vectors are denoted by t and s as in Section 2). If the facets of γ^{\boxtimes} do not lie in a single hyperplane, the normal n is averaged as the normalized sum of the piecewise constant approximations of the gradient of the level set function φ on all adjacent regular tetrahedra. Let $\mathcal{V}^{\text{local}}[T, z, n]$ denote the space of functions, which are affine on both sides of the plane $H := \{x \in \mathbb{R}^3 \mid (x - z) \cdot n = 0\}$ and which fulfill (2.5). We easily verify that the functions

$$\begin{aligned} \eta^0(x) &:= \begin{cases} K^n (x - z) \cdot n & \text{for } x \in H_+ \\ (x - z) \cdot n & \text{for } x \in H_- \end{cases}, \\ \eta^1(x) &:= \begin{cases} K^s (x - z) \cdot n + (x - z) \cdot s & \text{for } x \in H_+ \\ (x - z) \cdot s & \text{for } x \in H_- \end{cases}, \\ \eta^2(x) &:= \begin{cases} K^t (x - z) \cdot n + (x - z) \cdot t & \text{for } x \in H_+ \\ (x - z) \cdot t & \text{for } x \in H_- \end{cases}, \\ \eta^3(x) &:= 1 \end{aligned} \quad (3.1)$$

form a basis of $\mathcal{V}^{\text{local}}[T, z, n]$, where $H_{\pm} := \{x \in \mathbb{R}^3 \mid \pm (x - z) \cdot n \geq 0\}$ denote the two half-spaces separated by H . In the simpler isotropic case we can replace K^n by the kink ratio $\kappa := a^-/a^+$ as defined before and set $K^s = K^t = 0$ in the above formulas.

Next, let us define the set of coefficients yielding a suitable approximation of a function $u \in C^0$ in $\mathcal{V}^{\text{local}}[T, z, n]$. Hence, we denote by $\mathcal{M}_{T, z, n}[u]$ the set of coefficient vectors $(\tilde{\alpha}^0, \dots, \tilde{\alpha}^3)$ which minimizes

$$\sum_{i=0, \dots, 3} \left(u(x_i) - \sum_{j=0, \dots, 3} \tilde{\alpha}^j \eta^j(x_i) \right)^2 \quad (3.2)$$

where the x_i are the vertices of the tetrahedron T . We will verify below that in the scalar isotropic case, there is a unique interpolation of any set of nodal values

$u(x_0), \dots, u(x_3)$ in $\mathcal{V}^{\text{local}}[T, z, n]$. Thus, the minimum is zero and the associated coefficient vector $(\alpha^0, \dots, \alpha^3)$ solves the linear system $u(x_i) = \sum_{j=0, \dots, 3} \alpha^j \eta^j(x_i)$ exactly for $i = 0, \dots, 3$. On the other hand, we will observe that in the case of anisotropic tensors a^\pm , there can be an affine solution space of dimension at least 1, and correspondingly not every set of nodal values $u(x_0), \dots, u(x_3)$ can be interpolated by a function in $\mathcal{V}^{\text{local}}[T, z, n]$. Hence, to select a unique coefficient vector $(\alpha^0, \dots, \alpha^3)$ for later use in the interpolation we define

$$(\alpha^0, \dots, \alpha^3) := \operatorname{argmin}_{(\tilde{\alpha}^j)_{j=0, \dots, 3} \in \mathcal{M}_{T, z, n}[u]} \sum_{j=0, \dots, 3} (\tilde{\alpha}^j)^2, \quad (3.3)$$

which is indeed unique because we minimize the Euclidian norm of $(\tilde{\alpha}_0, \dots, \tilde{\alpha}_3)$ over the affine subspace $\mathcal{M}_{T, z, n}[u]$. The local evaluation of this approximation at the interface point z is then defined as

$$\mathcal{P}_{T, z, n}[u] := \sum_{j=0, \dots, 3} \alpha^j \eta^j(z). \quad (3.4)$$

Interpolation Operator. Once we have constructed $\mathcal{P}_{T, z, n}$ on each tetrahedron $T \in \mathcal{G}^\boxtimes$ intersecting the interface γ^\boxtimes , we can construct a global interpolation via local averaging in the vicinity of the interface. Indeed, we define $\mathcal{I}[u] : C^0 \rightarrow \mathcal{V}^\Delta$ via

$$\mathcal{I}[u](v) := \begin{cases} \frac{1}{\operatorname{card}\{T \in \mathcal{G}^\boxtimes \mid v \in T\}} \sum_{T \ni v} \mathcal{P}_{T, v, n(v)}[u] & \text{for } v \in \mathcal{N}^\Delta \setminus \mathcal{N}^\square, \\ u(v) & \text{for } v \in \mathcal{N}^\square. \end{cases} \quad (3.5)$$

Let us remark that the set $\{T \in \mathcal{G}^\boxtimes \mid z \in T\}$ is non-empty and its cardinality is bounded by 8. By construction, $\mathcal{I}[u]$ is determined solely by the values at nodes from the set of regular nodes \mathcal{N}^\square . An example of some CFE basis functions for an 2D scalar isotropic problem with kink ratio $\kappa = 10$ is shown in Fig. 3.3. Since for non-planar interfaces we determine an approximate interface and approximate normals for every virtual node, the interpolation $\mathcal{I}[u]$ fulfills the coupling condition (2.5) only approximately.

Composite Finite Element Basis Functions. Based on this interpolation we finally define the CFE basis functions and the CFE space

$$\psi_i^{\text{CFE}} := \mathcal{I}[\psi_i^\boxtimes], \quad \mathcal{V}^{\text{CFE}} := \operatorname{span} \{\psi_i^{\text{CFE}} \mid i \in I^\square\} \subset \mathcal{V}^\Delta. \quad (3.6)$$

In these definition the term ‘composite’ reflects the fact that the CFE basis functions ψ^{CFE} are composed of virtual basis functions ψ^Δ . In fact, for a regular node $x_i \in \mathcal{N}^\square$ we denote by $\mathcal{C}(x_i)$ the set of nodes $v \in \mathcal{N}^\Delta$ which lie in a regular tetrahedron with vertex x_i , v is then said to be ‘constrained’ by x_i . Then ψ_i^{CFE} is the linear combination of ψ_v^Δ for $v \in \mathcal{C}(x_i)$ (with weights $\mathcal{I}[\psi_i^\boxtimes](v)$). Let us list some properties of the CFE basis:

(i) Obviously, the ψ_i^{CFE} $i \in I^\square$ form a nodal basis, i.e. $u = \sum_{i \in I^\square} u(x_i) \psi_i^{\text{CFE}}$ for every $u \in \mathcal{V}^{\text{CFE}}$.

(ii) Away from the interface, there are no virtual nodes constrained by regular nodes, so the construction of CFE basis functions simply yields standard affine basis functions. Defined as a linear combination of virtual basis functions near the interface the CFE basis functions are piecewise affine.

(iii) A basis function ψ_i^{CFE} may have bigger support than ψ_i^\boxtimes since x_i may constrain virtual nodes z not lying on an edge whose end point is the corresponding

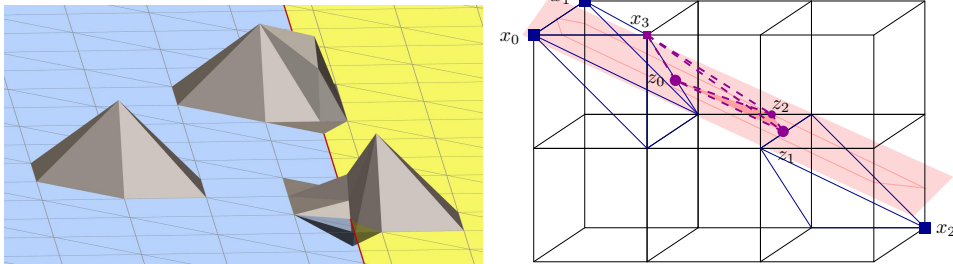


FIG. 3.3. On the left, 2D CFE basis functions for isotropic scalar diffusion with kink ratio $\kappa = 10$ are shown. Away from the interface (red line), CFE basis functions are identical to standard hat functions. At the interface, they may have larger (but still local) support and may attain negative values. On the right, we show an example for the possibly larger support of 3D CFE basis functions. A planar (transparent red plane) intersecting the regular grid \mathcal{G}^\square is depicted. The virtual node z_0 is constrained by the nodes x_0 and x_1 (among others) and the node z_1 is constrained by the node x_2 (among others), because each of the pairs z_0, x_0 and z_1, x_1 are node pairs of tetrahedra (solid blue) of the regular grid \mathcal{G}^\square . Furthermore, there is a local auxiliary tetrahedron T (dashed magenta) of \mathcal{G}^Δ with nodes x_3, z_0, z_1, z_2 . Hence, $T \subset \text{supp } \psi_{\{0,1\}}^{\text{CFE}} \cap \text{supp } \psi_2^{\text{CFE}}$ which implies that the supports of the CFE basis functions corresponding the nodes x_0 and x_2 (on the same side of the interface) and x_1 and x_2 (on different sides of the interface) overlap.

regular node. Indeed, for such a node z with index j , $\text{supp}(\psi_j^\Delta) \not\subset \text{supp}(\psi_i^\square)$, and thus $\text{supp}(\psi_i^{\text{CFE}}) = \text{supp}(\psi_i^\Delta) \cup \bigcup_{j \in \mathcal{C}(x_i)} \text{supp}(\psi_j^\Delta)$ with $\mathcal{C}(x_i)$ defined as above. For geometric reasons, however, the support of a basis function is contained in a ball with diameter $6h$ with respect to the maximum norm. In fact, for two nodes in the support the distance can be at most two times the distance between regular and virtual node plus the maximal distance between two virtual nodes of the same local auxiliary tetrahedron (cf. Fig. 3.3 for an example configuration). Let us remark that in 2D the bound is smaller and supports of basis functions are contained in balls with diameter $4h$ in the maximum norm.

(iv) A basis function ψ_i^{CFE} may attain negative values and values greater than 1. Furthermore, it need not satisfy the coupling condition (2.5) across γ^\square pointwise.

Existence of a Unique Nodal Interpolation in $\mathcal{V}^{\text{local}}$ in the Isotropic Scalar Case. If the minimum set $\mathcal{M}_{T,v,n(v)}[u]$ of the least square problem (3.2) consists of a single coefficient vector and the minimum is zero, then there exists a unique $v \in \mathcal{V}^{\text{local}} = \mathcal{V}^{\text{local}}[T, z, n]$ with the same x_i -nodal values as u . Thus, we can equivalently consider the problem of finding weights $\omega^0, \dots, \omega^3$ solving the interpolation problem in $\mathcal{V}^{\text{local}}$, which—expressed in terms of the basis $(\eta^j)_{j=0,\dots,3}$ —leads to the linear system of equations

$$\eta^j(z) = \omega^0 \eta^j(x_0) + \omega^1 \eta^j(x_1) + \omega^2 \eta^j(x_2) + \omega^3 \eta^j(x_3) \quad (3.7)$$

for $j = 0, \dots, 3$. From the last equation for $\eta^3 \equiv 1$ we deduce that the weights always sum up to 1. As a consequence, we observe that the CFE basis forms a partition of unity because the nodal basis on \mathcal{V}^Δ does. Let us remark that even though the weights sum up to 1, they may lie outside $[0, 1]$ and thus in general do not define a convex combination, which is due to the fact that the η^j are not globally affine. In this case, we can write the approximation problem (3.4) as the interpolation problem

$$\mathcal{P}_{T,z,n}[u] = \sum_{i=0,\dots,3} \omega^i u(x_i) \quad (3.8)$$

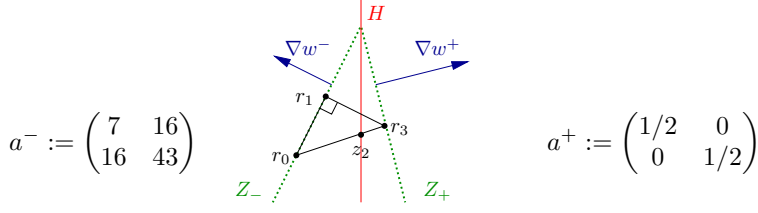


FIG. 3.4. Illustration of the counterexample for unique solvability of the construction system (3.7).

at the point z .

Let us now demonstrate that in the scalar isotropic case, equation (3.7) is uniquely solvable. To see this, we verify that the linear mapping $I : \mathcal{V}^{\text{local}} \rightarrow \mathbb{R}^4$, $u \mapsto (u(x_i))_{i=0, \dots, 3}$ is bijective. Preimage and image space have the same dimension, hence it is sufficient to verify the injectivity. Without loss of generality let us assume that x_0, x_1 are on one side and x_3 on the other side of the planar local interface approximation H as defined for (3.1) (x_2 may be on either side). Moreover, assume that z_2, z_3 are two points on H such that the tetrahedron (x_0, x_1, z_2, z_3) is non-degenerate. If I is not injective, there exists $w \in \mathcal{V}^{\text{local}}$ with $w \neq 0$ with $I(w) = 0$. Without loss of generality let us assume that $w(z_2) \neq 0$. The sets $Z_{\pm} := [w = 0] \cap H_{\pm}$ are thus of codimension 1, i.e. planes parallel to H or halfplanes on one side of the interface not containing z_2 . In the parallel case, the straight line through z_2 in normal direction n obviously intersects Z_- and Z_+ , which implies a sign change of $\partial_n w$ at z_2 , contradicting the coupling condition (2.5) in the scalar isotropic case. In the non-parallel case, continuity implies that $Z_- \cap H = Z_+ \cap H$ is a line. Since the angles formed by the edges of the regular tetrahedron (x_0, x_1, x_2, x_3) in \mathcal{G}^{\boxtimes} are bounded from above by 90° (see Fig. 3.1) and its vertices lie in $Z_- \cup Z_+$, also the angle between the halfplanes Z_- and Z_+ is bounded by 90° . This implies that the straight line through z_2 in normal direction n on H in fact still intersects the halfplanes Z_- and Z_+ , leading to the same contradiction as before.

As already mentioned, in general equation (3.7) is not uniquely solvable in the scalar anisotropic case, as shown by the following counterexample. Let us first consider the 2D setting shown in Fig. 3.4. Positive definiteness of a^- and a^+ is easily verified. Moreover, let $H := [x = 0]$, $n = (0, 1)^T$, $t = (1, 0)^T$, and $w^-(x, y) := -2x + y$, $w^+(x, y) := 4x + y$. The resulting function w and its tangential derivatives are clearly continuous across γ and the coupling condition is also satisfied, since

$$\begin{aligned} a^- \nabla w^- n &= \begin{pmatrix} 7 & 16 \\ 16 & 43 \end{pmatrix} \begin{pmatrix} -2 \\ 1 \end{pmatrix} \cdot \begin{pmatrix} 1 \\ 0 \end{pmatrix} = \begin{pmatrix} 2 \\ 11 \end{pmatrix} \cdot \begin{pmatrix} 1 \\ 0 \end{pmatrix} = 2, \\ a^+ \nabla w^+ n &= \begin{pmatrix} 1/2 & 0 \\ 0 & 1/2 \end{pmatrix} \begin{pmatrix} 4 \\ 1 \end{pmatrix} \cdot \begin{pmatrix} 1 \\ 0 \end{pmatrix} = \begin{pmatrix} 2 \\ 1/2 \end{pmatrix} \cdot \begin{pmatrix} 1 \\ 0 \end{pmatrix} = 2. \end{aligned}$$

The sets $Z_{\pm} := [w^{\pm} = 0]$ are two rays starting at the origin perpendicular to ∇w^{\pm} . Due to $\angle(\nabla w^-, \nabla w^+) > 90^\circ$ and $\angle(Z^-, Z^+) < 90^\circ$, a triangle x_0, x_1, x_2 with $x_0, x_1 \in Z^+$, $x_2 \in Z^-$ with a 90° angle and catheti of the same length exists. Let $z := [x_0, x_2] \cap H$, then $w(z) \neq 0$ (w is zero at the origin but nowhere else on H) even though $w(x_i) = 0$ for $i = 0, 1, 2$. Constant extension in the third space direction, a corresponding modification of the two diffusion tensors a^{\pm} , and a fourth vertex x_3 lying above x_0 turns this into a 3D example with a regular tetrahedron with vertices x_i and $w(x_i) = 0$ for $i = 0, \dots, 3$, then $w \in \mathcal{V}^{\text{local}}[T, z, n]$ does *not* imply $w(z) = 0$.

3.3. Composite Basis Functions for Linearized Elasticity. The construction of a CFE basis in the vector value case of linearized elasticity is performed in analogy to the scalar case in Section 3.2 above, however some bookkeeping of the additional indices is required.

Local Interpolation Scheme. The coupling condition (2.9) implies that the set of locally admissible displacement profiles is spanned by the following 12 displacement functions $\{\eta^{i,j}\}_{i=0,\dots,3, j=0,1,2}$ (here the index i corresponds to the same index as in the scalar case (3.1), whereas j refers to the j th vector component)

$$\begin{aligned} \eta^{0,j}(x) &:= \begin{cases} (x-z) \cdot n K_j^n & \text{for } x \in H_+ \\ (x-z) \cdot n e_j & \text{for } x \in H_- \end{cases}, \\ \eta^{1,j}(x) &:= \begin{cases} (x-z) \cdot n K_j^s + (x-z) \cdot s e_j & \text{for } x \in H_+ \\ (x-z) \cdot s e_j & \text{for } x \in H_- \end{cases}, \\ \eta^{2,j}(x) &:= \begin{cases} (x-z) \cdot n K_j^t + (x-z) \cdot t e_j & \text{for } x \in H_+ \\ (x-z) \cdot t e_j & \text{for } x \in H_- \end{cases}, \\ \eta^{3,j}(x) &:= e_j. \end{aligned} \quad (3.9)$$

Here, e_j is the j th canonical basis vector in \mathbb{R}^3 and A_j represents the j th column of the matrix $A = (A_{ij})_{i,j=0,1,2}$ for $A = K^n$, K^s , and K^t , respectively. $H_\pm := \{x \in \mathbb{R}^3 \mid \pm(x-z) \cdot n \geq 0\}$ are defined as above. Let us again denote the space of admissible vector-valued, piecewise affine functions fulfilling the coupling condition (2.9) by $\mathcal{V}^{\text{local}}[T, z, n]$.

In analogy to the scalar case, let $\mathcal{M}_{T,z,n}[u]$ to be the set of coefficient vectors $(\tilde{\alpha}^{k,j})_{k=0,1,2, j=0,\dots,3} \in \mathbb{R}^9$ minimizing (cf. (3.2))

$$\sum_{i=0,\dots,3} \left| u(x_i) - \sum_{\substack{k=0,1,2 \\ j=0,\dots,3}} \tilde{\alpha}^{k,j} \eta^{k,j}(x_i) \right|^2 \quad (3.10)$$

where $|\cdot|$ is the Euclidian norm. As in (3.3) we extract the unique coefficient vector

$$(\alpha^{k,j})_{k=0,1,2, j=0,\dots,3} := \underset{(\tilde{\alpha}^{k,j}) \in \mathcal{M}_{T,z,n}[u]}{\operatorname{argmin}} \sum_{\substack{k=0,1,2 \\ j=0,\dots,3}} \|\tilde{\alpha}^{k,j}\|_{\mathbb{F}}^2 \quad (3.11)$$

so that we can evaluate the associated approximation of a function $u \in (C^0)^3$ in $\mathcal{V}^{\text{local}}[T, z, n]$ at the interface point z as (cf. (3.4))

$$\mathcal{P}_{T,z,n}[u] := \sum_{\substack{k=0,1,2 \\ j=0,\dots,3}} \alpha^{k,j} \eta^{k,j}. \quad (3.12)$$

Again, if the minimum set $\mathcal{M}_{T,v,n(v)}[u]$ consists of a single coefficient vector with zero minimum, we can equivalently consider the interpolation problem in $\mathcal{V}^{\text{local}}[T, z, n]$ of finding $\omega^0, \dots, \omega^3 \in \mathbb{R}^{3 \times 3}$ solving (cf. (3.7))

$$\eta_l^{k,j}(z) = \sum_{\substack{m=0,\dots,3 \\ n=0,1,2}} \omega_{ln}^m \eta_n^{k,j}(x_m) \quad (3.13)$$

for $k = 0, 1, 2$, $j = 0, \dots, 3$, and all components $l = 0, 1, 2$. We can then write (3.12) as the interpolation problem (cf. (3.8))

$$\mathcal{P}_{T,z,n}[u] = \left(\sum_{\substack{l=0,\dots,3 \\ n=0,1,2}} \omega_{nk}^l u_n(x_l) \right)_{k=0,1,2}. \quad (3.14)$$

However, the scalar uniqueness proof can straightforwardly be extended to the isotropic elasticity case only if $\nu = 0$ ($\lambda = 0$). For discontinuous ν and E , again counterexamples exist.

Vector-Valued Composite Finite Element Basis Functions. Based on the evaluation $\mathcal{P}_{T,z,n}[u]$ of the local approximation, we proceed as in the scalar case in Section 3.2 and define the global interpolation $\mathcal{I}[u] : (C^0)^3 \rightarrow \mathcal{V}^\Delta$ by the formulas (3.5), except that the resulting interpolation is a vector-valued function. Finally, a CFE basis in the vector-valued case and the CFE space are (cf. (3.6))

$$\psi_{ik}^{\text{CFE}} := \mathcal{I}[\psi_i^\boxtimes e_k], \quad \mathcal{V}^{\text{CFE}} := \text{span} \{ \psi_{ik}^{\text{CFE}} \mid i \in I^\square, k = 0, 1, 2 \}. \quad (3.15)$$

Note that $\psi_i^\boxtimes e_k$ discretizes the displacement in a single space direction whereas ψ_{ik}^{CFE} (near the interface) may have contributions in all space directions. Again, ψ_{ik}^{CFE} are composed of virtual basis functions $\psi_v^\Delta e_k$ for all $v \in \mathcal{C}(x_i)$ and for $k = 0, 1, 2$ by linear combination, where $\mathcal{C}(x_i)$ is defined as before.

4. Sketch of the Algorithm and Implementational Issues. In this section we comment on some implementational issues. For a comprehensive description of the mesh generation and the processing of the interface described by level sets, we refer to [53].

Grid Handling and Data Storage. In the algorithm, neither \mathcal{G}^\boxtimes nor \mathcal{G}^Δ are stored explicitly. Instead when traversing the mesh, for every cell we compute its *signature*, i.e. the signs of the level set function φ at the vertices. The local mesh topology of \mathcal{G}^Δ solely depends on this signature. Hence, given a signature of a mesh cell we can extract the local interface topology from a lookup table, which is parameterized by the signature of mesh cells. Via suitable scaling the actual intersection of the interface with grid lines is taken into account and a local matrix assembly is performed. Obviously, during the mesh traversal, the geometric configuration around a virtual node $z \in \mathcal{N}^\Delta \setminus \mathcal{N}^\square$ has to be retrieved for every tetrahedron containing z . To allow a reuse of data describing the local geometry of \mathcal{G}^Δ and the involved weights, in different tetrahedra, we store them in an standard template library (STL) map data structure. The sorted concatenated (64 bit) pair of the two (32 bit) indices of the end points of the edge containing z are used as the key to retrieve the corresponding data items from the STL data structure.

Robust Computation of the Construction Weights. The construction of the CFE basis functions requires, for each auxiliary node $z \in \mathcal{N}^\Delta \setminus \mathcal{N}^\square$ and every tetrahedron $T \in \mathcal{G}^\Delta$, the computation of K^n , K^s , K^t defined as coefficients in (2.7) for the scalar case or matrices in (2.10) for the vector-valued case and of the set of weights w^i or weight matrices $w^l = (w_{nk}^l)_{nk}$ (in the exact interpolation cases (3.8) and (3.14)). Depending on the relative location of the auxiliary node z on the edge and on the ratio between the coefficients on both sides of the interface (κ in the scalar isotropic case), this can lead to an ill-conditioned problem. Especially the linear systems of equations (3.7) and (3.13) can be difficult to solve accurately in particularly degenerate cases. Hence, tetrahedra leading to such degenerate cases are detected and the corresponding

contributions to the averaging process in (3.5) are skipped for the computation of the interpolation value. Denoting the numerical inverse computed in finite precision by $A^{\sim 1}$, we distinguish between *reliable* and *unreliable* regular tetrahedra depending on whether $\|AA^{\sim 1} - \text{Id}\|_F$ for the matrix in one of the involved linear systems is smaller than some threshold. For the solution of (3.13) we use the norm of the residuum as reliability measure. The threshold must be chosen small enough to prevent unreliable tetrahedra from contributing numerical errors to the CFE construction, but also big enough to allow at least one reliable tetrahedron per virtual node. In fact, we start e.g. with a threshold of $2 \cdot 10^{-15}$ and increase it globally if there are virtual nodes for which no reliable tetrahedron is found. Let us also mention that in our computations no configuration of tetrahedron T and virtual z with interface normal n occurred for which least squares problem (3.2) or (3.10) were degenerate in the sense that no interpolant existed. Hence, we effectively solved the associated interpolation problems via (3.7) or (3.13).

Assembling Matrices. For assembling global matrices, we loop over hexahedra of \mathcal{G}^\square and iterate over the corresponding tetrahedra $T \in \mathcal{G}^\Delta$ in the these hexahedra. If a hexahedron is intersected by the interface, the local matrix entries are obtained from a lookup table, weighted according to the values of the CFE basis functions, and finally assembled into the global matrix. If the interface γ^\boxtimes does not intersect the hexahedron (indicated by a signature consisting of constant sign), we are in the standard configuration of piecewise affine FE on the tetrahedral mesh \mathcal{G}^\boxtimes . Again, the local FE matrix is retrieved from a fixed lookup table, scaled with the appropriate powers of the grid size and assembled into the global matrix.

Solvers and Preconditioners. We use a preconditioned conjugate gradient (PCG) solver with SSOR preconditioning [34]. For the vector-valued elasticity problem, a block variant [34] of SSOR is used, where 3×3 blocks are considered corresponding to nodal displacement vectors.

Although uniform hexahedral grids contain canonical coarse scales, and thus are candidates for geometric multigrid solvers [87, 80], these cannot easily be integrated into the 3D CFE context (cf. [67]). Different interface resolutions at different mesh levels lead to the problem that a coarsening scheme needs to simultaneously preserve the partition of unity property and prevent artificial kinks in the basis functions away from the interface. Thus, the design and implementation of a specialized CFE multigrid method, possibly in combination with algebraic multigrid methods [75, 27] still requires further investigation.

Memory Requirements. Due to the fact that CFE basis functions are associated with nodes of \mathcal{G}^\square , the memory requirement for a data vectors on a $(2^l)^3$ grid is $O(2^{3l})$. The total memory requirement to handle the data for a single virtual node is typically about 300 bytes in the scalar case and 750 bytes in the vector-valued case. If we assume that our interface is a smooth hypersurface, we deal with $O(2^{2l})$ interface nodes. Without any regularity assumption on the interface, the worst bound on the number of virtual nodes is the number of regular edges, which is $O(2^{3l})$.

Both the time for the matrix assembly and the memory required to store a global FE matrix scales essentially linearly in the number of interface nodes. Here, we take into account that (if the coefficient is constant throughout a subdomain) matrix entries corresponding to nodes apart from the interface can be retrieved from a lookup table not only when assembling matrices but also when computing matrix-vector products. The storage requirement for the lookup tables is negligible at about 2 MB.

The sparsity structure of CFE matrices is determined by the local geometry of

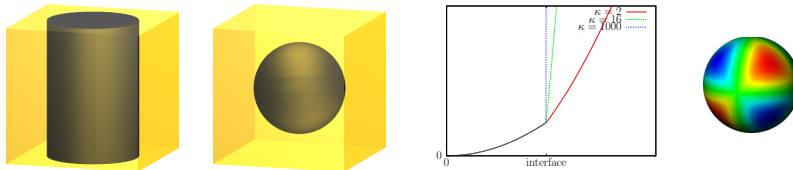


FIG. 5.1. The figures shows two cylindrically and spherically symmetric objects (left). On rays through the center, we use the one-dimensional piecewise smooth prototype function admitting different kink ratios (second from right), where the test function for the sphere is multiplied by a tangential modulation term (right).

\mathcal{G}^Δ . In the scalar case, a matrix row has 15 entries for nodes apart from the interface (as for piecewise affine FE) on \mathcal{G}^\boxtimes and up to 89 entries for nodes near the interface. In case of a underlying regular grid with 129^3 nodes on grid level $l = 7$ for the bone specimen A in Fig. 6.5, approximately 619 MB are required to store one CFE matrix (in the scalar case), where 90.1 % of the rows are explicitly stored.

Parallelization. For current shared-memory multi-core or multi-processor computers, a straightforward parallelization of the code allows a significant speed-up at low implementational effort. Indeed, SSOR preconditioning and matrix-vector multiplications in the solution step are easily parallelized based on an appropriate ordering of the degrees of freedom, using OpenMP in our C++ implementation.

5. CFE Simulation for Composite Materials. Let us now present numerical results obtained with the proposed CFE method. Subsection 5.1 deals with a study of the grid convergence of the approximation of given functions and the solution of elliptic boundary value problems. In Subsections 5.2 and 5.3, we show results of heat conduction and elasticity simulations, respectively.

5.1. Approximation Properties. On the real line we consider prototype functions which admit kinks of different ratios (cf. Fig. 5.1). From these we construct cylindrically and spherically symmetric functions, respectively, whose approximation with the CFE basis functions is studied. In the case of the cylindrical interface the function is constant along the interface, in the case of the spherical interface we also multiply by a tangential modulation which is shown in Fig. 5.1 as well. In both cases, we compare the resulting analytically given function, which is piecewise smooth, with its CFE interpolant. We evaluate the L^2 and H^1 approximation error by midpoint quadrature over \mathcal{G}^Δ and L^∞ approximation error by examining all grid and quadrature points. For varying kink ratio between 1 (no kink) and 10^7 , we observe second and first order convergence in the L^2 and H^1 norms for decreasing mesh size, respectively, where the approximate convergence rates lie within $[1.95, 2.01]$ (L^2) and $[1, 1.18]$ (H^1) for h decreasing from 2^{-2} to 2^{-9} . The L^∞ approximation error exhibits stable convergence rates in $[1.85, 2.01]$ for the cylindrical example. However, for the spherical test case the L^∞ error suffers from outliers and lies within $[1.1, 2.2]$. The result of our study for selected kink ratios $\kappa \in \{2, 16, 1000\}$ is reported in Fig. 5.2. In addition, we here compare the CFE method to a standard affine FE scheme without any adaptation to the curved interface. From our numerical investigations we see that the convergence of our CFE method is improved by approximately one order in the L^∞ norm and by approximately half an order in the integrated L^2 and H^1 norms compared to standard affine FE.

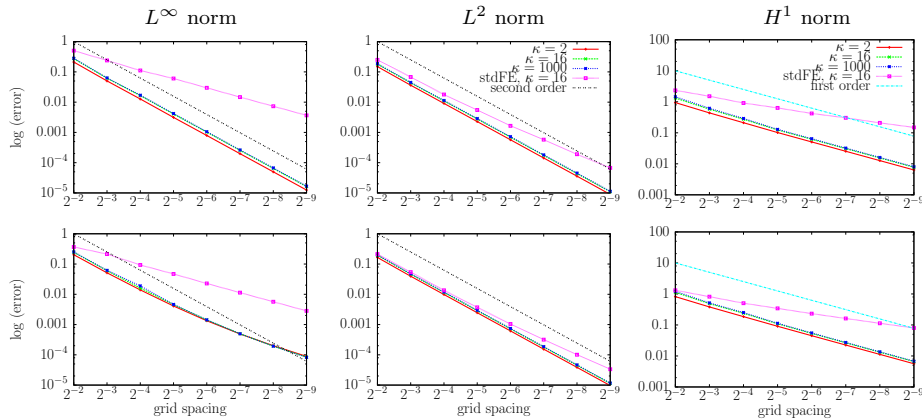
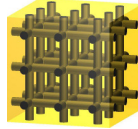


FIG. 5.2. The plots show the convergence of the CFE approximation error of cylindrically symmetric (middle row) and tangentially modulated cylindrically symmetric (bottom row) functions for different kink ratios $\kappa \in \{2, 16, 1000\}$, measured in the L^∞ , L^2 , and H^1 norms (from left to right), relative to the L^2 norm of the function. For comparison, we also plot the expected optimal order of convergence and the convergence of the error for standard affine interpolation (stdFE, for kink ratio $\kappa = 16$) on the hexahedral grid, thus ignoring the kink and attaining orders 1.0, 1.5, and 0.5 only.



h	scalar problem			elasticity problem		
	L^∞ error	L^2 error	H^1 error	L^∞ error	L^2 error	H^1 error
1/16	0.055279	0.008245	0.359515	0.266884	0.007583	0.564360
1/32	0.023502	0.003393	0.193077	0.108070	0.003046	0.268633
1/64	0.009512	0.001092	0.097312	0.051376	0.000939	0.121923
1/128	0.004850	0.000348	0.048578	0.049559	0.000230	0.056526
1/256	0.002119	0.000090	0.023283			

FIG. 5.3. Numerical consistency analysis for a scalar and an elasticity boundary value problem on the domain shown on the left.

Numerical Consistency of Boundary Value Problems. Furthermore, we consider the 3^3 rod interface shown in Fig. 5.3. For this configuration we compute the solutions of a scalar boundary value problem (isotropic coefficient, kink ratio $\kappa = 42$) and an elasticity problem (compression in z direction, material parameters $E = 5$, $\nu = 0.2$ in the rods and $E = 1$, $\nu = 0.2$ in the remaining matrix). The solutions are computed at different resolution and compared to a ‘reference solution’, which is obtained at grid resolution 513^3 (scalar problem) and 257^3 (elasticity problem). We evaluate the L^∞ , L^2 , and H^1 norm of the difference via midpoint quadrature on the finest \mathcal{G}^Δ . In the elasticity case, pointwise Euclidian and Frobenius norm are used for differences of the vector-valued quantity and its derivatives, respectively.

We observe in both problems that the convergence behavior in L^∞ is clearly below second order whereas convergence in L^2 is close to second order and in H^1 , we have almost perfect first order convergence.

5.2. Heat Conduction Simulation. Let us now consider a sample of aluminium foam (Al) embedded in polymethylmethacrylate (PMMA), on which we simulate the temporal evolution of temperature. The edge length of the sample is 7.71 mm and the computational hexahedral grid contains 257^3 nodes. We use realistic volume-

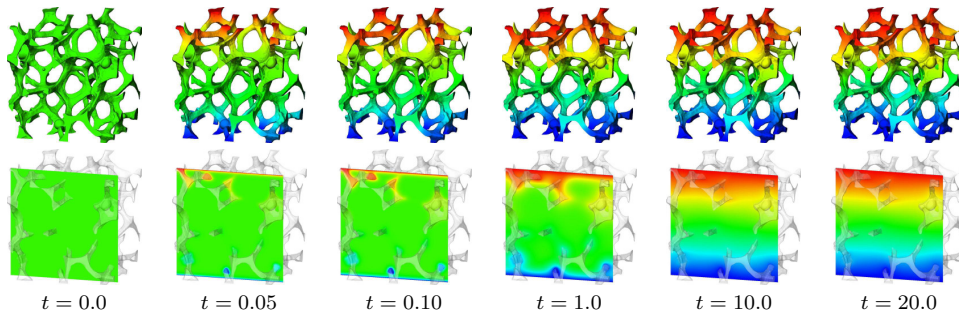


FIG. 5.4. Heat conduction simulation on an Al foam embedded in PMMA. Temperatures (194.65 K 373.15 K) are visualized on the interface (top row) and on a slice through the composite material (bottom row). The temperature profiles for different times show that an almost steady state is reached much faster in the metal than in the plastic.

specific heat capacities $\rho c = \{2.43, 1.75\} \cdot 10^6$ J/m³ K and thermal conductivities of $\lambda = \{237.0, 0.19\}$ W/m K for Al and PMMA, respectively. Thus, the thermal conductivity has a kink ratio of $\kappa \approx 1247$. The initial condition is set to room temperature 293.15 K and boundary conditions are 194.65 at the bottom and 373.15 K at the top. For the time-stepping an implicit Euler scheme is used. Results of the computation are depicted in Fig. 5.4.

5.3. Linear Elasticity Simulation. Finally, we simulate elasticity of objects with a complicated internal structure. First the Al/PMMA structure from the last paragraph is considered with realistic stiffness parameters $E = 70$ GPa, $\nu = 0.35$ and $E = 3$ GPa, $\nu = 0.38$. Now the object is resolved at 120 μm , resulting in a 65^3 computational grid. In Fig. 5.5 we show the result of a simulation of torsion by 1 degree.

The second sample is part of a porcine T1 vertebral body for which we assume the elasticity parameters $E = 13$ GPa and $\nu = 0.32$. These microscopic material parameters are realistic for human vertebral bodies [86], whose pore size, however, is bigger than the one for pigs. The object is scanned at 35 μm resolution, resulting in a $143 \times 143 \times 214$ computational grid. We assume the specimen to be filled with PMMA as above ($E = 3$ GPa, $\nu = 0.38$) and simulate a compression in longitudinal direction by 1 percent. Again the results are shown in Fig. 5.5. Note that both deformations are scaled by a factor of 20 to enhance the visual perception.

6. Numerical Homogenization Based on CFE. In what follows we aim at computing macroscopic diffusion tensors and elasticity tensors for microstructured composite materials. As in the above simulations, the material is supposed to be described via 3D images of prototype structures or actual material specimens.

First, we consider the case of a periodic domain corresponding to material with a regular periodic structures. However, real material specimens in general can not be considered as cells of a periodic lattice. We will thus, in a second step, adapt the homogenization approach for periodic domains to structures which are supposed to be prototype cells in a statistical sense. Numerical experiments demonstrate that the proposed modification actually allows to extract macroscopic properties of the underlying composite material in a reliable fashion.

6.1. Cell Problems for Periodic Domains. At first, let us briefly review how to evaluate an effective, homogenized material property based on a corrector problem

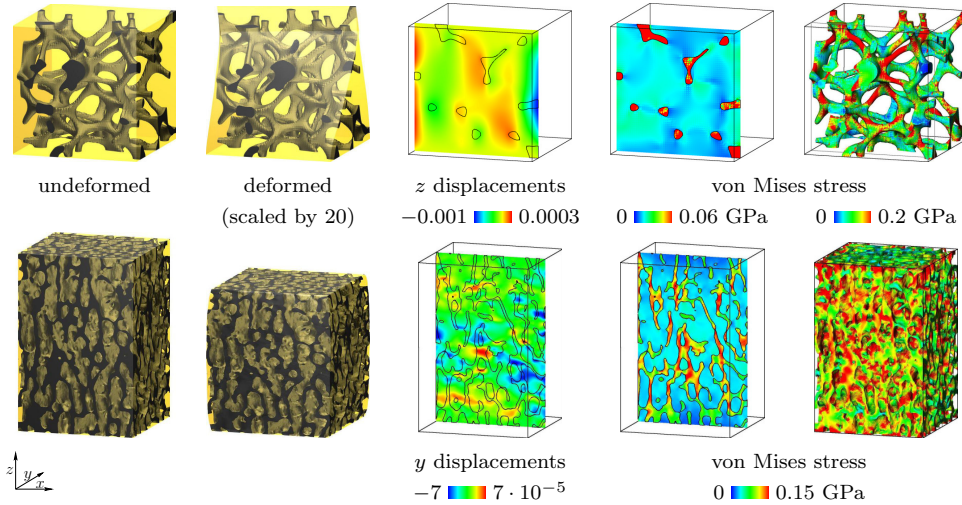


FIG. 5.5. Top: *Linear elasticity simulation on Al foam/PMMA dataset: torsion by 1° (scaled by a factor of 20). Besides undeformed and deformed structure, we show on a slice ($y = 1/6$; in the undeformed configuration) the induced z displacements and the von Mises stress on a slice through the object and (for the Al structure) on the interface, making visible the effect of the 23-fold stiffness of the Al foam.* Bottom: *1 % compression of a porcine trabecular bone / PMMA dataset. The effect of four times higher stiffness of the bone is visible in the y displacements and the von Mises stresses on a slice. Note that in both examples the deformations have been scaled by a factor of 20.*

on the fundamental cell of a periodic domain. For details we refer to [2, Chapter 1]. An implementation in the context of a CFE element method for complicated domains but with continuous coefficient can be found in [69].

Scalar Model Problem. Given the scalar problem (2.2) on a macroscopic domain Ω with an underlying periodic lattice and a fundamental cell $\Omega^\# = [0, 1]^3$, we consider a splitting $u = \tilde{u} + \bar{u}$ of the solution u into a microscopic quantity \tilde{u} reflecting the microscopic fluctuations and a macroscopic quantity \bar{u} . We suppose that \tilde{u} satisfies periodic boundary conditions on $\partial\Omega^\# = [0, 1]^3$ and that $\int_{\Omega^\#} \tilde{u} \, dx = 0$, whereas \bar{u} is considered to be affine on $\Omega^\#$. From (2.2) we deduce that

$$\int_{\Omega^\#} a \nabla \tilde{u} \cdot \nabla v \, dx = - \int_{\Omega^\#} a \nabla \bar{u} \cdot \nabla v \, dx \quad \forall v \in H_{\#}^{1,2}(\Omega^\#), \quad (6.1)$$

which can be used to solve for \tilde{u} for any given \bar{u} . $H_{\#}^{1,2}(\Omega^\#)$ here denotes the space $H^{1,2}(\Omega^\#)$ restricted to functions which fulfill periodic boundary conditions.

The effective diffusion tensor $\bar{a} = (\bar{a}_{ij})_{ij}$ describes the relation between macroscopic gradient and macroscopic heat flux via $\bar{q} = \bar{a} \nabla \bar{u}$ where the macroscopic flux is evaluated on the fundamental cell as $\bar{q} = \int_{\Omega^\#} a \nabla u \, dx = \int_{\Omega^\#} a \nabla (\bar{u} + \tilde{u}) \, dx$. Choosing \bar{u}^i with $\nabla \bar{u}^i = e_i$ for $i = 0, 1, 2$ and denoting by \tilde{u}^i the corresponding solution of (6.1) and by \bar{q}^i the corresponding macroscopic flux, we obtain $\bar{a}_{ij} = \bar{q}_i^j = \bar{q}^j \cdot e_i$. Even though in the spatially continuous case the resulting homogenized diffusion tensor \bar{a} is symmetric, we observe a slight lack of symmetry for the numerically computed tensor, which vanishes in the asymptotic limit for successively refined meshes. Hence, it turns out to be numerically more convenient to use the—in the spatially continuous

case—equivalent variational definition

$$\int_{\Omega^\#} \bar{a} \nabla \bar{u} \cdot \nabla \bar{u} = \inf_{\tilde{v} \in H_{\#}^{1,2}(\Omega)} \int_{\Omega^\#} a \nabla(\bar{u} + \tilde{v}) \cdot \nabla(\bar{u} + \tilde{v}) \quad (6.2)$$

for a symmetric tensor \bar{a} . This definition leads to the same Euler-Lagrange equation as (6.1). The minimum in (6.2) is attained by \tilde{u} solving (6.1) for given \bar{u} . Hence, the entries \bar{a}_{ik} of \bar{a} are obtained taking into account that $a_{ik} = ae_i \cdot e_k = ae_{i+k} \cdot e_{i+k} - ae_{i-k} \cdot e_{i-k}$ for symmetric a and for $e_{i\pm k} := \frac{1}{2}(e_i \pm e_k)$. Indeed, for \bar{u}^i with $\nabla \bar{u}^i = e_i$ we finally obtain

$$\begin{aligned} \bar{a}_{ik} &= \int_{\Omega^\#} \bar{a} \nabla \bar{u}^i \cdot \nabla \bar{u}^k = \int_{\Omega^\#} \bar{a} \nabla \bar{u}^{i+k} \cdot \nabla \bar{u}^{i+k} - \bar{a} \nabla \bar{u}^{i-k} \cdot \nabla \bar{u}^{i-k} \\ &= \int_{\Omega^\#} a \nabla(\bar{u}^{i+k} + \tilde{u}^{i+k}) \cdot \nabla(\bar{u}^{i+k} + \tilde{u}^{i+k}) - a \nabla(\bar{u}^{i-k} + \tilde{u}^{i-k}) \cdot \nabla(\bar{u}^{i-k} + \tilde{u}^{i-k}), \end{aligned} \quad (6.3)$$

where $\nabla \bar{u}^{i\pm k} = \frac{1}{2}(e_i \pm e_k)$ and $\tilde{u}^{i\pm k}$ is the corresponding solution of (6.1).

Linearized Elasticity. In the vector-valued case of linearized elasticity, the displacement u is, in analogy to (6.1), decomposed into a macroscopic displacement \bar{u} and a microscopic displacement component \tilde{u} with periodic boundary conditions and $\int_{\Omega^\#} \tilde{u} \, dx = 0$ solving

$$\int_{\Omega} C \epsilon(\tilde{u}) : \epsilon(v) \, dx = - \int_{\Omega} C \epsilon(\bar{u}) : \epsilon(v) \, dx \quad \forall v \in H_{\#}^{1,2}(\Omega, \mathbb{R}^3) \quad (6.4)$$

due to (2.8). The effective elasticity tensor $\bar{C} = (\bar{C}_{ijkl})_{ijkl}$ now couples macroscopic strain $\epsilon(\bar{u})$ and stress $\bar{\sigma}$ via $\bar{\sigma} = \bar{C} \epsilon(\bar{u})$. Here, the effective stress is evaluated as $\bar{\sigma} = \int_{\Omega^\#} C \epsilon(\bar{u} + \tilde{u}) \, dx$, and we have to consider at least 6 (due to symmetry of stress and strain) macroscopic displacements $\bar{u}_0, \dots, \bar{u}_5$ with linearly independent strain tensors $e_{ij} := \epsilon(\bar{u}^{ij}) = \frac{1}{2}(e_i \otimes e_j + e_j \otimes e_i)$ for $i, j \in \{0, 1, 2\}$ and $i \leq j$. Then, we achieve $\bar{C}_{\cdot ij} = \sigma^{ij} := \int_{\Omega^\#} C(\epsilon(\tilde{u}^{ij}) + e_{ij}) \, dx$, where \tilde{u}^{ij} solves (6.4) for given \bar{u}^{ij} . Again, we take into account the variational formulation (cf. (6.2))

$$\int_{\Omega^\#} \bar{C} \epsilon(\bar{u}) : \epsilon(\bar{u}) = \inf_{\tilde{v} \in H_{\#}^{1,2}(\Omega; \mathbb{R}^3)} \int_{\Omega^\#} C \epsilon(\bar{u} + \tilde{v}) : \epsilon(\bar{u} + \tilde{v}) \quad (6.5)$$

leading to the same Euler-Lagrange equation as (6.4) for the minimum \tilde{u} given the macroscopic displacement \bar{u} .

Hence the entries \bar{C}_{ijkl} of the symmetric tensor \bar{C} are obtained using the formula $C_{ijkl} = Ce_{ij} : e_{kl} = \frac{1}{4}(Ce_{ij+k} : e_{ij+k} - Ce_{ij-k} : e_{ij-k})$ for given microscopic elasticity tensor C , $e_{ij\pm kl} := \frac{1}{2}(e_{ij} \pm e_{kl})$, and \bar{u}^{ij} with $\epsilon(\bar{u}^{ij}) = e_{ij}$. Indeed, we obtain

$$\begin{aligned} \bar{C}_{ijkl} &= \int_{\Omega^\#} \bar{C} \epsilon(\bar{u}^{ij}) : \epsilon(\bar{u}^{kl}) \, dx \\ &= \int_{\Omega^\#} \bar{C} \epsilon(\bar{u}^{ij+kl}) : \epsilon(\bar{u}^{ij+kl}) - \bar{C} \epsilon(\bar{u}^{ij-kl}) : \epsilon(\bar{u}^{ij-kl}) \, dx \\ &= \int_{\Omega^\#} C \epsilon(\bar{u}^{ij+kl} + \tilde{u}^{ij+kl}) : \epsilon(\bar{u}^{ij+kl} + \tilde{u}^{ij+kl}) \\ &\quad - C \epsilon(\bar{u}^{ij-kl} + \tilde{u}^{ij-kl}) : \epsilon(\bar{u}^{ij-kl} + \tilde{u}^{ij-kl}) \, dx \end{aligned} \quad (6.6)$$

where $\epsilon(\bar{u}^{ij\pm kl}) = \frac{1}{2}(e_{ij} \pm e_{kl})$ and $\tilde{u}^{ij\pm kl}$ is the corresponding solution of (6.4).

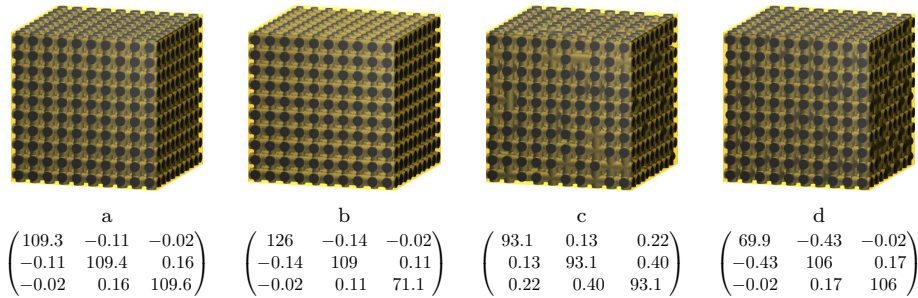


FIG. 6.1. Numerical homogenization of heat diffusion and elasticity is applied to periodic material samples. (b is a full $10 \times 10 \times 10$ structure of cylindrical rods with diameter/length ratios 0.38, 1/3, 0.24 in the different space directions (a), (c), (d) have diameter/length ratios 1/3 in each space direction where (a), (b) are full structures, (c) is missing (randomly chosen) 10 percent of the connections (in each space direction), and (d) is missing 30 percent of the connections in x direction only.

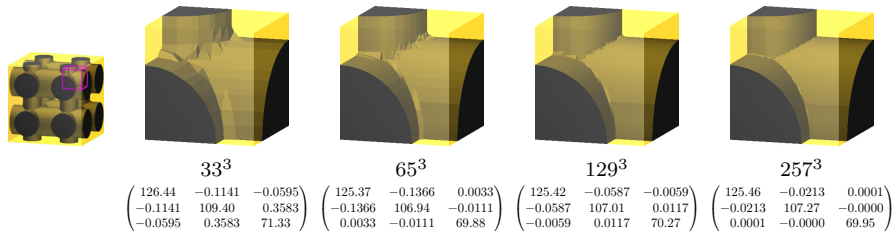


FIG. 6.2. For $2 \times 2 \times 2$ rods of diameter/length ratios 0.38, 0.33, 0.24 (left), we show a zoom to one trabecular crossing at different computational resolutions ranging from 33^3 to 257^3 grid nodes, along with the numerically homogenized heat conductivity tensors obtained at the different resolutions.

Periodic Boundary Conditions. We implement periodic boundary conditions by the usual identification of nodes on opposite boundary faces of the fundamental cell $\Omega^\#$ and a corresponding merging of the corresponding basis functions. Furthermore, a projecting preconditioned conjugate gradient method takes into account the constraint $\int \tilde{u} dx = 0$.

Homogenization of a Scalar Model Problem. For the scalar case of heat conduction, we consider a periodic cell problem where the fundamental cell is covered by a 3D lattice structure consisting of $10 \times 10 \times 10$ cylindrical rods. We study different diameter/length ratios in the three space directions and the case where a part of the rods is randomly removed. The selected ratio of 237 : 0.19 between the two diffusion coefficients reflects realistic values for aluminium and PMMA. In Fig. 6.1 we report the resulting homogenized heat conductivity tensor. In Fig. 6.2 we furthermore study the convergence for increasing spatial resolution.

Homogenization of an Elasticity Model Problem. Next, we investigate homogenization in the context of linearized elasticity. In a first numerical experiment we again consider the object (b) in Fig. 6.1 having an edge length of 1 m and with an underlying regular grid having 129^3 nodes. For the (microscopically) isotropic linear elasticity parameters for Al ($E = 13$ GPa, $\nu = 0.32$) and PMMA ($E = 3$ GPa, $\nu = 0.38$) we obtain the homogenized elasticity tensor in Voigt's notation (see e.g. [20])

in units of GPa

$$C = \begin{bmatrix} 12.386 & 5.768 & 5.571 & & & \\ 5.768 & 11.927 & 5.499 & & & \\ 5.571 & 5.499 & 11.152 & & & \\ & & & 2.520 & & \\ & & & & 2.644 & \\ & & & & & 2.937 \end{bmatrix}$$

where entries with absolute value smaller than 10^{-3} times the maximal entry have been omitted.

Furthermore, we study a fundamental cell with a 3D trabecular structure, which is rotated in the (y, z) plane by an angle $\alpha = \arctan(1/5) \approx 11.310^\circ$, see Fig. 6.4. The geometry is constructed in such a way that there is a smooth periodic extension. Here, the edge length is 1 m, $E = 10$ Pa and $\nu = 0.1$ inside the structure, $E = 1$ Pa and $\nu = 0.3$ in the surrounding matrix. For the computations we use an underlying regular grid with 65^3 .

Once the homogenized elasticity tensor C is computed, we determine a rotation matrix $Q = (Q_{ab})_{ab}$ such that the appropriately rotated elasticity tensor minimizes the non-orthotropy defect with respect to the canonical coordinate system in the Frobenius norm. Following [82, 89] this means a numerical minimization of

$$F(Q) = \frac{\|R_a[Q_{mi}Q_{nj}Q_{pk}Q_{ql}C_{ijkl}]\|_F^2}{\|R_b[Q_{mi}Q_{nj}Q_{pk}Q_{ql}C_{ijkl}]\|_F^2} \quad (6.7)$$

where R_a is the restriction to the entries not present in an orthotropic tensor and R_b the restriction to those present (upper left block and diagonal of lower right block).

For the example considered here we obtain a rotation by -11.289° in the (y, z) -plane, almost perfectly recovering the geometric rotation. The resulting elasticity tensors C and its back-rotated version $C^{-\alpha}$ are

$$C = \begin{bmatrix} 1.822 & 0.607 & 0.606 & & & \\ 0.607 & 1.794 & 0.630 & -0.049 & & \\ 0.606 & 0.630 & 1.803 & 0.050 & & \\ & -0.049 & 0.050 & 0.485 & & \\ & & & & 0.465 & \\ & & & & & 0.463 \end{bmatrix} \quad C^{-\alpha} = \begin{bmatrix} 1.822 & 0.607 & 0.607 & & & \\ 0.607 & 1.815 & 0.610 & & & \\ 0.607 & 0.610 & 1.823 & & & \\ & & & 0.465 & & \\ & & & & 0.465 & \\ & & & & & 0.463 \end{bmatrix}$$

where, as above, small entries have been omitted.

6.2. Statistical Prototype Cell Problems. Let us now assume that a material specimen contains a (rescaled) cubic cell $\Omega^\#$, which is considered to be a statistical prototype realization of the material structure.

In a straightforward manner one might be tempted to periodize the material by simple mirroring in all space directions and thereby constructing a new fundamental domain consisting of eight copies of the initial cube $\Omega^\#$. This approach can clearly introduce artificial axial anisotropy and may destroy existing anisotropy. Simply applying periodic boundary conditions in case of non-periodic media will not work either, since this means identifying points on the boundary with different material parameters leading to inconsistent geometric structures.

A better approach is obtained by replacing the periodic boundary conditions by a Dirichlet boundary condition $u = \bar{u}$ on $\partial\Omega^\#$, where \bar{u} is again supposed to be affine. In case of a periodic sample the solution of this modified cell problem will be strongly impacted by the artificial boundary conditions. In fact compared to the realistic case of physically natural periodic boundary conditions the Dirichlet boundary condition in (6.4) lead to an artificial stiffening in a layer around the boundary of the cell.

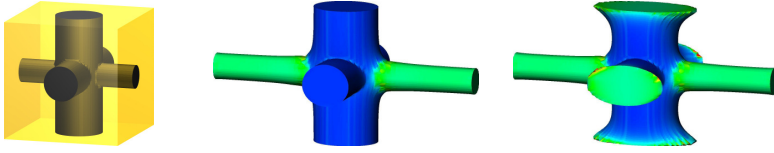


FIG. 6.3. For a $1 \times 1 \times 1$ rod dataset, the difference between periodic (middle) and Dirichlet (right) boundary conditions is shown for one tensile loading case. Dirichlet boundary conditions prevent the longitudinal rods from thinning at the boundary and force the transverse rods to an elliptic cross section at the boundary, leading to higher average stress for the same macroscopic strain. Color encodes the von Mises stress at the interface.

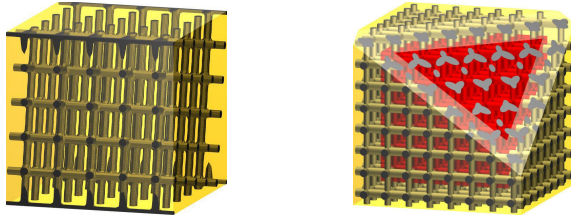


FIG. 6.4. The left picture shows an orthotropic object rotated by $\arctan(1/5)$ so that its orthotropy axes are not aligned with the coordinate axes. In the right pictures, the evaluation subdomain $\Omega_{1/8}^\#$ used in the homogenization approach for not necessarily periodic domains are highlighted, while the simulation is performed on the whole domain. One corner of the object has been clipped to enhance the visualization.

This fact is illustrated in Fig. 6.3 where we compare the physically correct solution with periodic boundary conditions with the case, where (artificial) Dirichlet boundary conditions are imposed.

To reduce the influence of these boundary artifacts, fluxes q or stresses σ are averaged over a subdomain $\Omega_\beta^\# := \{x \in \Omega^\# \mid \text{dist}(x, \partial\Omega^\#) > \beta\}$ only, with $\beta \in (0, 1)$. Thus we evaluate (6.2) and (6.5) on $\Omega_\beta^\#$ only. The proper choice of β can be tedious. On the one hand, for decreasing β the impact of the boundary layer is increased. On the other hand, for large values of β and fixed experimental material specimen the statistical properties of the material are possibly no longer well represented on the smaller domain $\Omega_\beta^\#$.

To evaluate the effect of the Dirichlet boundary condition and the parameter β on the homogenized effective parameter, we perform the following numerical experiment: A structure with $8 \times 8 \times 8$ cylindrical rods of diameter-to-length ratios 0.4, 0.35, and 0.3 in x , y , and z direction, respectively, with microscopically isotropic lattice material properties ($E = 10$ Pa, $\nu = 0.1$) is embedded into a matrix with $E = 1$ Pa, $\nu = 0.3$, see Fig. 6.4. The domain of extent 1 m^3 is resolved by a regular grid with 129^3 grid nodes. Applying the homogenization method for periodic domains, we obtain the macroscopic elasticity tensor in Pa

$$C = \begin{bmatrix} 2.698 & 0.652 & 0.650 & & & \\ 0.652 & 2.505 & 0.649 & & & \\ 0.650 & 0.649 & 2.314 & & & \\ & & & 0.581 & & \\ & & & & 0.611 & \\ & & & & & 0.642 \end{bmatrix}$$

Using the numerical homogenization method with Dirichlet boundary conditions

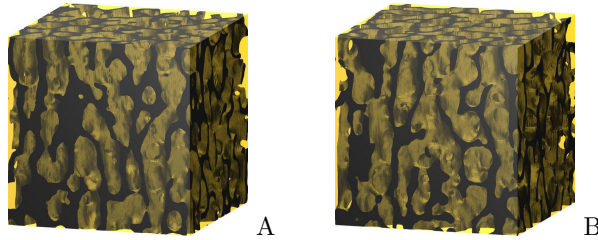


FIG. 6.5. Two cubic specimens of a porcine T1 vertebral body are shown at 35 μm resolution (part of the ones shown in Fig. 5.5) used for numerical homogenization on statistically periodic cells.

with $\beta = 0$ and $\beta = 1/8$, respectively, the resulting elasticity tensors are

$$C^{\beta=0} = \begin{bmatrix} 2.713 & 0.652 & 0.651 & & & \\ 0.652 & 2.525 & 0.649 & & & \\ 0.651 & 0.649 & 2.337 & & & \\ & & & 0.609 & & \\ & & & & 0.641 & \\ & & & & & 0.673 \end{bmatrix}, \quad C^{\beta=\frac{1}{8}} = \begin{bmatrix} 2.698 & 0.652 & 0.650 & & & \\ 0.652 & 2.505 & 0.649 & & & \\ 0.650 & 0.649 & 2.314 & & & \\ & & & 0.592 & & \\ & & & & 0.624 & \\ & & & & & 0.657 \end{bmatrix}$$

Obviously, for the evaluation of the effective stresses on the whole domain $\Omega^\#$ for $\beta = 0$ boundary artifacts in fact play a significant role. Leaving out a boundary layer of one pore size (in this case $\beta = \frac{1}{8}$) almost completely eliminates this effect. Further numerical experiments confirm that larger boundary layers do not improve the result significantly, at the cost of using only a small portion of the domain on which the simulation needs to be run.

The following table lists the Frobenius norm of the difference between the tensors obtained with periodic boundary conditions and Dirichlet boundary conditions, where we restrict the norm-computation to the entries appearing in an orthotropic tensor.

boundary layer β	0/8	1/8	2/8	3/8
Frobenius difference (relevant entries)	0.108	0.045	0.029	0.020
relative DOF usage	1.000	0.422	0.125	0.016

The numbers show that the difference decreases with increasing boundary layer, along with the number of nodes used for evaluation divided by the number of nodes used in the simulation.

Homogenized Elasticity of Trabecular Bone. Finally, we consider two different cubic subsets of the single (porcine) bone specimen (cf. Fig. 6.5) and assume the same material parameters as before ($E = 13$ GPa, $\nu = 0.32$ in the bone, $E = 3$ GPa, $\nu = 0.38$ in the PMMA). The cubic domain $\Omega^\#$ is resolved by a 129^3 regular grid.

Following [39], the domain $\Omega_\beta^\#$ is sufficiently large if it covers at least five pore sizes in each direction. Thus for the value $\beta = \frac{1}{8}$ chosen here we are in the range of a representative cell problem in the sense of [39].

For the specimen A in Fig. 6.5, we obtain in Voigt's notation and in units of GPa

$$C = \begin{bmatrix} 8.369 & 4.585 & 4.575 & & & \\ 4.585 & 8.424 & 4.587 & -0.017 & & \\ 4.575 & 4.587 & 9.040 & -0.059 & & \\ & & & -0.057 & 1.996 & 0.033 \\ -0.012 & & & 0.034 & 1.990 & -0.020 \\ 0.061 & 0.075 & 0.018 & & -0.020 & 1.897 \end{bmatrix}, \quad C^Q = \begin{bmatrix} 8.250 & 4.594 & 4.560 & & & \\ 4.594 & 8.519 & 4.598 & -0.012 & -0.098 & -0.014 \\ 4.560 & 4.598 & 9.055 & & & \\ & & & -0.012 & 2.025 & \\ & & & -0.098 & & 1.958 \\ & & & -0.014 & & 1.903 \end{bmatrix}$$

as the efficient elasticity tensor and its rotation C^Q by roll, pitch, and yaw angles 7.37, 2.16, and -40.99 degrees. The rotation Q is obtained by the same optimization

already discussed above. Hence, C^Q is the best approximation to an orthotropic elasticity tensor in a rectangular coordinate system. We observe that the trabecular bone material is almost orthotropic.

For specimen B in Fig. 6.5, we obtain

$$C = \begin{bmatrix} 7.929 & 4.433 & 4.427 & & & 0.030 \\ 4.433 & 8.072 & 4.442 & & & 0.053 \\ 4.427 & 4.442 & 8.629 & -0.029 & & \\ & & -0.029 & 1.879 & 0.021 & \\ & & & 0.021 & 1.863 & -0.012 \\ 0.030 & 0.053 & & & -0.012 & 1.783 \end{bmatrix} \quad C^Q = \begin{bmatrix} 7.902 & 4.422 & 4.424 & & & \\ 4.422 & 8.120 & 4.444 & & & \\ 4.424 & 4.444 & 8.633 & & & \\ & & & 1.890 & 0.009 & \\ & & & 0.009 & 1.851 & \\ & & & & & 1.772 \end{bmatrix}$$

where C^Q again represents a transformed elasticity tensor with rotation angles 3.82, 7.26, and -25.12 . We observe that the two homogenized elasticity tensors from samples A and B are very similar. This can be considered as an indication for the fact that the specimen is statistically homogeneous with respect to the overall stress-strain relation but not with respect to the orientation of the anisotropy. Homogenization results for these two specimens are meant as proof of concept, a more detailed biomechanical study of trabecular structures of different species is ongoing research.

Acknowledgments. Ole Schwen was supported by the DFG project RU567/8-2 ‘Multiscale Simulation and Validation of the Elastic Microstructures of Vertebral Bodies’. The authors thank Hans-Joachim Wilke and Uwe Wolfram at the Institute for Orthopaedic Research and Biomechanics, University of Ulm, for inspiring discussions and for providing the μ CT scan datasets of the aluminium foam and bone specimens and the Hausdorff Center for Mathematics, University of Bonn, for providing computational resources. Moreover, we would like to thank Benedikt Wirth for fruitful discussions on the CFE construction.

REFERENCES

- [1] L. Adams and Z. Li. The immersed interface / multigrid methods for interface problems. *SIAM J. Sci. Comput.*, 24(2):463–479, 2002.
- [2] G. Allaire. *Shape optimization by the homogenization method*, volume 146 of *Applied Mathematical Sciences*. Springer-Verlag, New York, 2002.
- [3] T. Arbogast. *Numerical Treatment of Multiphase Flows in Porous Media*, volume 552 of *Lecture Notes in Physics*, chapter Numerical Subgrid Upscaling of Two-Phase Flow in Porous Media, pages 35–49. Springer, 2000.
- [4] T. Arbogast. *Current Trends in Scientific Computing*, chapter An overview of subgrid upscaling for elliptic problems in mixed form, pages 21–32. Contemporary Mathematics. AMS, 2003.
- [5] T. Arbogast, S. E. Minkoff, and P. T. Keenan. *Computational Methods in Contamination and Remediation of Water Resources*, volume 1 of *Computational Methods in Water Resources*, chapter An operator-based approach to upscaling the pressure equation, pages 405–412. Computational Mechanics Publications, 1998.
- [6] G. P. Astrakhantsev. Method of fictitious domain for a second-order elliptic equation with natural boundary conditions. *U.S.S.R. Computational Mathematics and Mathematical Physics*, 18:114–121, 1978.
- [7] I. Babuška, U. Banerjee, and J. E. Osborn. Survey of meshless and generalized finite element methods: A unified approach. *Acta Numer.*, 12:1–125, 2003.
- [8] I. Babuška and J. M. Melenk. The partition of unity method. *Internat. J. Numer. Methods Engrg.*, 40:727–758, 1997.
- [9] J. W. Barrett and C. M. Elliott. Fitted and unfitted finite-element methods for elliptic equations with smooth interfaces. *IMA J. Numer. Anal.*, 7:283–300, 1987.
- [10] J. W. Barrett and C. M. Elliott. A practical finite element approximation of a semi-definite Neumann problem on a curved domain. *Numer. Math.*, 51:23–36, 1987.
- [11] T. Belytschko and T. Black. Elastic crack growth in finite elements with minimal remeshing. *Internat. J. Numer. Methods Engrg.*, 45(5):601–620, 1999.
- [12] T. Belytschko, N. Moës, S. Usui, and C. Parimi. Arbitrary discontinuities in finite elements. *Internat. J. Numer. Methods Engrg.*, 50(4):993–1013, 2001.

- [13] M. Bern and D. Eppstein. *Computing in Euclidian Geometry*, volume 1 of *Lecture Notes Series on Computing*, chapter Mesh generation and optimal triangulation, pages 23–90. World Scientific, Singapore, 1992.
- [14] R. P. Beyer and R. J. LeVeque. Analysis of a one-dimensional model for the immersed boundary method. *SIAM J. Numer. Anal.*, 29(2):332–364, 1992.
- [15] A. E. Brandt. Methods of systematic upscaling. Technical Report MCS06-05, Weizmann Institute of Science, 2006.
- [16] D. Calhoun and R. J. LeVeque. A Cartesian grid finite-volume method for the advection-diffusion equation in irregular geometries. *J. Comput. Phys.*, 157:143–180, 2000.
- [17] M. C. Chang, C. L. Liu, and T. H. Chen. Polymethylmethacrylate augmentation of pedicle screw for osteoporotic spinal surgery: a novel technique. *Spine*, 33(10):E317–E324, 2008.
- [18] S.-I. Chen, R.-M. Lin, and C.-H. Chang. Biomechanical investigation of pedicle screw – vertebrae complex: a finite element approach using bonded and contact interface conditions. *Medical Engineering & Physics*, 25:275–282, 2003.
- [19] C. Daux, N. Moës, J. Dolbow, N. Sukumar, and T. Belytschko. Arbitrary branched and intersecting cracks with the extended finite element method. *Internat. J. Numer. Methods Engrg.*, 48:1741–1760, 2000.
- [20] C. Decolon. *Analysis of Composite Structures*. Taylor & Francis, 2000.
- [21] C. A. Duarte, I. Babuška, and J. T. Oden. Generalized finite element methods for three-dimensional structural mechanics problems. *Computers & Structures*, 77:215–232, 2000.
- [22] C. A. Duarte, O. N. Hamzeh, T. J. Liszka, and W. W. Tworzydło. A generalized finite element method for the simulation of three-dimensional dynamic crack propagation. *Comput. Methods Appl. Mech. Engrg.*, 190:2227–2262, 2001.
- [23] C. A. Duarte, D.-J. Kim, and D. M. Quaresma. Arbitrarily smooth generalized finite element approximations. *Comput. Methods Appl. Mech. Engrg.*, 196:33–56, 2006.
- [24] A. Düster, J. Parvizian, Z. Yang, and E. Bank. The finite cell method for three-dimensional problems of solid mechanics. *Comput. Methods Appl. Mech. Engrg.*, 197(45–48):3768–3782, August 2008.
- [25] K. Eriksson, D. Estep, P. Hansbo, and C. Johnson. Introduction to adaptive methods for differential equations. *Acta Numer.*, pages 105–158, 1995.
- [26] R. E. Ewing, R. D. Lazarov, T. F. Russell, and P. S. Vassilevski. Local refinement via domain decomposition techniques for mixed finite element methods with regular Raviart-Thomas elements. In T. F. Chan, R. Glowinski, J. Periaux, and O. B. Widlund, editors, *Proceedings of the Third International Symposium on Domain Decomposition Methods for Partial Differential Equations*, pages 98–114, Philadelphia, 1990. Society for Industrial and Applied Mathematics.
- [27] R. D. Falgout. An introduction to algebraic multigrid. Technical Report UCRL-JRNL-220851, Lawrence Livermore National Laboratory, 2006.
- [28] T. Gao, W. H. Zhang, J. H. Zhu, Y. J. Xu, and D. H. Bassir. Topology optimization of heat conduction problem involving design-dependent heat load effect. *Finite Elements in Analysis and Design*, 44(14):805–813, 2008.
- [29] L. J. Gibson. Biomechanics of cellular solids. *Journal of Biomechanics*, 38:377–399, 2005.
- [30] R. Glowinski and Y. Kuznetsov. Distributed Lagrange multipliers based on fictitious domain method for second order elliptic problems. *Computer Methods in Applied Mechanics and Engineering*, 196:1498–1506, 2007.
- [31] Y. Guéguen, M. Le Ravalec, and L. Ricard. Upscaling: Effective medium theory, numerical methods and the fractal dream. *Pure and Applied Geophysics*, 163:1175–1192, 2006.
- [32] R. M. Gulrajani. The forward and inverse problems of electrocardiography. *IEEE Engineering in Medicine and Biology*, 17(5):84–101, 1998.
- [33] Y. Guo, M. Oritz, T. Belytschko, and E. A. Repetto. Triangular composite finite elements. *Internat. J. Numer. Methods Engrg.*, 47:287–316, 2000.
- [34] W. Hackbusch. *Iterative Solution of Large Sparse Systems of Equations*, volume 95 of *Applied Mathematical Sciences*. Springer, 1994.
- [35] W. Hackbusch and S. A. Sauter. Composite finite elements for problems containing small geometric details. Part II: Implementation and numerical results. *Computing and Visualization in Science*, 1(1):15–25, 1997.
- [36] W. Hackbusch and S. A. Sauter. Composite finite elements for the approximation of PDEs on domains with complicated micro-structures. *Numer. Math.*, 75:447–472, 1997.
- [37] W. Hackbusch and S. A. Sauter. A new finite element approach for problems containing small geometric details. *Archivum Mathematicum*, 34:105–117, 1998. Equadiff 9 issue.
- [38] A. Hansbo and P. Hansbo. An unfitted finite element method, based on nitsche’s method, for elliptic interface problems. *Comput. Methods Appl. Mech. Engrg.*, 191:5537–5552, 2002.

- [39] T. P. Harrigan, M. Jasty, R. W. Mann, and W. H. Harris. Limitations of the continuum assumption in cancellous bone. *Journal of Biomechanics*, 21(4):269–275, 1988.
- [40] K. Höllig, C. Apprich, and A. Streit. Introduction to the Web-method and its applications. *Adv. Comput. Math.*, 23:215–237, 2005.
- [41] K. Höllig, U. Reif, and J. Wipper. Weighted extended B-spline approximation of Dirichlet problems. *SIAM J. Numer. Anal.*, 39(2):442–462, 2001.
- [42] S. J. Hollister, D. P. Fyhrie, K. J. Jepsen, and S. A. Goldstein. Application of homogenization theory to the study of trabecular bone mechanics. *Journal of Biomechanics*, 24(9):825–839, 1991.
- [43] S. J. Hollister and N. Kikuchi. A comparison of homogenization and standard mechanics analyses for periodic porous composites. *Comput. Mech.*, 10:73–95, 1992.
- [44] T. Y. Hou and X.-H. Wu. A multiscale finite element method for elliptic problems in composite materials and porous media. *Journal of Computational Physics*, 134:169–189, 1997.
- [45] R. Huang, N. Sukumar, and J.-H. Prévost. Modeling quasi-static crack growth with the extended finite element method. Part II: Numerical applications. *Internat. J. Solids Structures*, 40(26):7539–7552, 2003.
- [46] M. A. Hyman. Non-iterative numerical solution of boundary value problems. *Applied Scientific Research, Section B*, 2:325–351, 1952.
- [47] V. Kosmopoulos and T. S. Keller. Damage-based finite-element vertebroplasty simulations. *European Spine Journal*, 13:617–625, 2004.
- [48] R. J. LeVeque and Z. L. Li. The immersed interface method for elliptic equations with discontinuous coefficients and singular sources. *SIAM J. Numer. Anal.*, 31(4):1019–1044, 1994.
- [49] Z. Li. A note on immersed interface method for three-dimensional elliptic equations. *Comput. Math. Appl.*, 31(3):9–17, February 1996.
- [50] Z. Li. The immersed interface method using a finite element formulation. *Appl. Numer. Math.*, 27:253–267, 1998.
- [51] Z. Li. An overview of the immersed interface method and its applications. *Taiwanese J. Math.*, 7(1):1–49, March 2003.
- [52] Z. Li, T. Lin, and X. Wu. New Cartesian grid methods for interface problems using the finite element formulation. *Numer. Math.*, 1996(1):61–98, November 2003.
- [53] F. Liehr, T. Preusser, M. Rumpf, S. Sauter, and L. O. Schwen. Composite finite elements for 3D image based computing. *Comput. Vis. Sci.*, 12(4):171–188, April 2009.
- [54] W. E. Lorensen and H. E. Cline. Marching cubes: A high resolution 3D surface construction algorithm. *Computer Graphics*, 21(4):163, 1987.
- [55] A.-M. Matache and C. Schwab. Two-scale FEM for homogenization problems. *Mathematical Modelling and Numerical Analysis*, 36(4):537–572, 2002.
- [56] J. M. Melenk. *On Generalized Finite Element Methods*. PhD thesis, University of Maryland, 1995.
- [57] W. F. Mitchell. A comparison of adaptive refinement techniques for elliptic problems. *ACM Trans. Math. Software*, 15(4):326–347, 1989.
- [58] J. D. Moulton, J. E. Dendy Jr., and J. M. Hyman. The black box multigrid numerical homogenization algorithm. *J. Comput. Phys.*, 142:80–108, 1998. Article No. CP985911.
- [59] J. T. Oden, C. A. M. Duarte, and O. C. Zienkiewicz. A new cloud-based hp finite element method. *Comput. Methods Appl. Mech. Engrg.*, 153:117–126, 1998.
- [60] S. J. Osher and J. A. Sethian. Fronts propagating with curvature dependent speed: Algorithms based on Hamilton–Jacobi formulations. *J. Comput. Phys.*, 79:12–49, 1988.
- [61] J. Parvizian, A. Düster, and E. Rank. Finite cell method. *Comput. Mech.*, 41(1):121–133, 2007.
- [62] A. Pegoretti, L. Fambri, G. Zappini, and M. Bianchetti. Finite element analysis of a glass fibre reinforced composite endodontic post. *Biomaterials*, 23(13):2667–2682, July 2002.
- [63] I. Ramière, P. Angot, and M. Belliard. A fictitious domain approach with spread interface for elliptic problems with general boundary conditions. *Comput. Methods Appl. Mech. Engrg.*, 196:766–781, 2007.
- [64] M. Rech, S. Sauter, and A. Smolianski. Two-scale composite finite element method for Dirichlet problems on complicated domains. *Numer. Math.*, 102:681–708, 2006.
- [65] A. Rohlmann, T. Zander, and G. Bergmann. Spinal loads after osteoporotic vertebral fractures treated by vertebroplasty or kryoplasty. *European Spine Journal*, 15:1255–1264, 2006.
- [66] V. K. Saul’ev. On solution of some boundary value problems on high performance computers by fictitious domain method. *Siberian Mathematical Journal*, 4:912–925, 1963.
- [67] S. A. Sauter and R. Warnke. Composite finite elements for elliptic boundary value problems with discontinuous coefficients. *Computing*, 77:29–55, 2006.
- [68] L. O. Schwen, T. Preusser, and M. Rumpf. Composite finite elements for 3D elasticity with

- discontinuous coefficients. In *Proceedings of the 16th Workshop on the Finite Element Method in Biomedical Engineering, Biomechanics and Related Fields*. University of Ulm, 2009. Accepted.
- [69] L. O. Schwen, U. Wolfram, H.-J. Wilke, and M. Rumpf. Determining effective elasticity parameters of microstructured materials. In *Proceedings of the 15th Workshop on the Finite Element Method in Biomedical Engineering, Biomechanics and Related Fields*, pages 41–62. University of Ulm, July 2008.
- [70] J. A. Sethian and A. Wiegmann. Structural boundary design via level set and immersed interface methods. *J. Comput. Phys.*, 163(2):489–528, 2000.
- [71] J. R. Shewchuk. What is a good linear element? Interpolation, conditioning, and quality measures. In *Proceedings of the 11th International Meshing Roundtable*, pages 115–126. Sandia National Laboratories, September 2002.
- [72] G. H. Shortley and R. Weller. The numerical solution of Laplace’s equation. *Journal of Applied Physics*, 9:334–344, May 1938.
- [73] M. Stolarska, D. L. Chopp, N. Moës, and T. Belytschko. Modelling crack growth by level sets in the extended finite element method. *Internat. J. Numer. Methods Engrg.*, 51:943–960, 2001.
- [74] T. Strouboulis, K. Copps, and I. Babuška. The generalized finite element method. *Comput. Methods Appl. Mech. Engrg.*, 190:4081–4193, 2001.
- [75] K. Stüben. A review of algebraic multigrid. *J. Comput. Appl. Math.*, 128:281–309, 2001.
- [76] L. Tartar. *Optimal Shape Design*, volume 1740 of *Lecture Notes in Mathematics*, chapter An Introduction to the Homogenization Method in Optimal Design, pages 47–156. Springer, 2001.
- [77] S.-H. Teng and C. W. Wong. Unstructured mesh generation: Theory, practice and applications. *Internat. J. Comput. Geom. Appl.*, 10(3):227–266, 2000.
- [78] P. Thoutireddy, J. F. Molinari, E. A. Repetto, and M. Ortiz. Tetrahedral composite finite elements. *Internat. J. Numer. Methods Engrg.*, 53(6):1337–1351, 2002.
- [79] G. M. Treece, R. W. Prager, and A. H. Gee. Regularized marching tetrahedra: improved iso-surface extraction. *Computers and Graphics*, 23(4):583–598, 1999.
- [80] U. Trottenberg, C. Osterlee, and A. Schüller. *Multigrid*. Academic Press, San Diego / London, 2001.
- [81] B. van Rietbergen, R. Müller, D. Ulrich, P. Rügsegger, and R. Huiskes. Tissue stresses and strain in trabeculae of canine proximal femur can be quantified from computer reconstructions. *Journal of Biomechanics*, 32:165–173, 1999.
- [82] B. van Rietbergen, A. Odgaard, J. Kabel, and R. Huiskes. Direct mechanics assessment of elastic symmetries and properties of trabecular bone architecture. *Journal of Biomechanics*, 29(12):1653–1657, 1996. Technical Note.
- [83] T. Vdovina, S. E. Minkoff, and O. Korostyshevskaya. Operator upscaling for the acoustic wave equation. *Multiscale Model. Simul.*, 4(4):1305–1338, 2005.
- [84] A. Wiegmann and K. P. Bube. The explicit-jump immersed interface method: Finite difference methods for pde with piecewise smooth solutions. *SIAM J. Numer. Anal.*, 37(3):827–862, 2000.
- [85] A. Wittek, R. Kikinis, S. K. Warfield, and K. Miller. Brain shift computation using a fully nonlinear biomechanical model. In J. Duncan and G. Gerig, editors, *Medical Image Computing and Computer-Assisted Intervention – MICCAI 2005*, volume 3750, pages 583–590, 2005.
- [86] U. Wolfram, H.-J. Wilke, and P. K. Zysset. Rehydration of vertebral trabecular bone: Influences on its anisotropy, its stiffness and the indentation work with a view to age, gender and vertebral level. *Bone*, 46:348–354, 2010.
- [87] J. Xu. *Theory of Multilevel Methods*. PhD thesis, Cornell University, May 1989.
- [88] W. Zhe, M. Hui, G. Manling, and G. Dong. A simulation of the abnormal EEG morphology by the 3-D finite element method. In *Proceedings of the 2005 IEEE Engineering in Medicine and Biology 27th Annual Conference*, pages 3620–3623, Shanghai, China, September 2005.
- [89] P. K. Zysset, R. W. Gullet, and S. J. Hollister. A global relationship between trabecular bone morphology and homogenized elastic properties. *Journal of Biomedical Engineering*, 120:640–646, 1999.